The Thesis Committee for Baiyuan Gao
Certifies that this is the approved version of the following thesis:

Pore Pressure within Dipping Reservoirs in Overpressured Basins

APPROVED BY
SUPERVISING COMMITTEE:

Supervisor:

Peter B. Flemings

John W. Snedden

Marc A. Hesse

Pore Pressure within Dipping Reservoirs in Overpressure Basins

by

Baiyuan Gao, B.S.

Thesis

Presented to the Faculty of the Graduate School of

The University of Texas at Austin

in Partial Fulfillment

of the Requirements

for the Degree of

Master of Science in Geological Sciences

The University of Texas at Austin

August 2013

Acknowledgements

I would like to express my sincere gratitude to my supervisor Dr. Peter Flemings, for his guidance, encouragement and continuous support while I am pursuing a master degree. Dr. Peter's enthusiasm for science, dedication to work, and persistent attitude for life have truly inspired me to reach my potential and pushed me to grow as a better geoscientist. I would also like to thank Dr. John Germaine, Dr. John Snedden and Dr. Marc Hesse for the valuable suggestions they gave me throughout my research.

I have been fortunate to work and receive guidance from my friendly and helpful "GeoFluidians". I would like to thank Michael Merrell and Andrew Smith for their help with Geolog and GMT. I thank Julia Reece and William Betts for their instructions and useful discussion of the lab experiments. I appreciate Maria Nikolinakou and Julia Reece for taking time in reviewing my thesis and reports. I also thank Maria Nikolinakou for teaching me to use geomechanical software. I have benefited from talking with Yao You about research ideas, software usage, and mathematical questions. I am grateful for knowing and learning from Michael Cronin, Gang Luo and Peter Polito. I would also like to thank Tessa Green for arranging appointment time for me within Dr. Peter's busy schedule and organizing numerous events for our group.

I acknowledge the sponsors of UT-Geofluids Consortium for providing me financial support. I especially thank Schlumberger for offering PetroMod and software training opportunity.

I thank my parents for giving me the opportunity to live, to learn and to pursue my dreams. Your exceptional love and support for each decision I have made has encouraged me throughout my life.

Abstract

Pore Pressure within Dipping Reservoirs in Overpressure Basins

Baiyuan Gao, M.S.Geo.Sci.

The University of Texas at Austin, 2013

Supervisor: Peter B. Flemings

A systematic study of how mudstone permeability impacts reservoir pore pressure is important to understand the regional fluid field within sedimentary basins and the control of sediment properties on subsurface pressure. I develop a 2D static model to predict reservoir overpressure from information estimated from the bounding mudstones and structural relief. This model shows that close to a dipping reservoir, the mudstone permeability is high in the up-dip location and low in the down-dip location. This characteristic mudstone permeability variation causes the depth where reservoir pressure equals mudstone pressure (equal pressure depth) to be shallower than the mid-point of the reservoir structure. Based on the 2D static model, I constructed a nomogram to determine the equal pressure depth by considering both farfield mudstone vertical effective stress and reservoir structural relief. I find the equal pressure depth becomes shallower with decreasing vertical effective stress, increasing reservoir structural relief, and increasing mudstone compressibility. Pressure predicted by the static model agrees with pressure predicted by a more complete model that simulates the evolution of the basin and is supported by field observations in the Bullwinkle Basin (Green Canyon 65, Gulf of

Mexico). This study can be applied to reduce drilling risk, analyze trap integrity, and facilitate safe and efficient exploration.

Table of Contents

List of Tables

List of Figures

Chapter 1: Pore Pressure within Dipping Reservoirs in Overpressured Basins

1.1 INTRODUCTION

Overpressure studies have generated significant attention among geoscientists for decades due to their applications in the interpretation of various geological phenomena, such as the occurrence of mud volcanoes (Reilly and Flemings, 2010; Van Rensbergen et al., 2005), sedimentary dikes (Cosgrove, 2001; Elsworth and Voight, 1995), landslides (Dugan and Flemings, 2002; Prior and Coleman, 1982; Stigall and Dugan, 2010), and earthquakes (Blanpied et al., 1992; Byerlee, 1990). For the oil and gas industry, the benefits of accurately predicting overpressure include the ability to design safe and economic wells, better understand hydrocarbon migration, and better predict trap integrity (Flemings and Lupa, 2004; Garenstroom et al., 1993; Hunt, 1990).

Overpressure can be generated by a wide range of mechanisms including mechanical loading by sedimentation (Brehoeft and Hanshaw, 1968; Harrison and Summa, 1991), hydrocarbon generation (Barker, 1990; Law and Spencer, 1998; Spencer, 1987), volume change of pore fluid due to temperature change (Barker, 1972; Powley, 1990), and diagenetic reactions that produce pore fluid (Bruce, 1984; Burst, 1969). In the Gulf of Mexico and other basins with rapid deposition of mudstone, it is generally agreed that overpressure is mainly generated by mechanical loading due to sedimentation (Gordon and Flemings, 1998; Harrison and Summa, 1991). High sedimentation rates, high sediment compressibility and low permeability result in inefficient drainage of pore fluids (Gibson, 1958). Under these conditions, the fluid supports part of the overlying load and pore pressure exceeds the hydrostatic pressure.

Recent work in the analysis of overpressured systems has emphasized how laterally continuous permeable aquifers within overpressured mudstones impact flow, pore pressure distribution, and geological processes. Dickinson (1953), first described how permeable aquifers will have a hydrostatic pore pressure gradient whereas the surrounding mudstone can have a higher pore pressure gradient. Flemings et al. (2002) documented this behavior with field examples and presented a model to describe how flow is focused along the permeable aquifer from regions of high pressure and large overburden stress towards regions of lower overpressure and less overburden stress. They showed that in many overpressured systems, the low permeability mudstone bounding the reservoir follows the lithostatic gradient whereas the reservoir, if permeable and well connected to regional sandstones, follows the hydrostatic gradient (e.g. **Fig. 1.1b**). Dugan and Flemings (2002) describe how this process can drive slope instability and Seldon and Flemings(2005) and Reilly and Flemings (2010) describe how this process impacts trap integrity and drives the expulsion of fluids through seafloor vents. Yardley and Swarbrick (2000) illustrate this process in two dimensional basin modeling.

One of the most practical, yet challenging, questions in pore pressure prediction is to determine what the pore pressure is within a large regional sand that is exposed to overpressured mudstone where the mudstone overpressure can vary substantially (**Fig. 1.1c**). It is critical in well design to be able to predict the pressure in the permeable reservoir because the fluid will flow into the well bore if pressures encountered are too high and lost circulation will occur if the pressures encountered are too low. Lupa and Flemings (2004) expanded on the work of Flemings et al. (2002) and Yardley and Swarbrick (2000) and suggested that under the conditions where the overpressure in the mudstone varied linearly with depth, the pore pressure within the aquifer could be estimated by determining the mudstone pressure at the area-averaged depth of the

sandstone. The approach can be applied in both two and three dimensions (Flemings and Lupa, 2004). This approach was grounded in theoretical modeling that demonstrated that rate of flow into the sand was controlled by the difference between the aquifer and the mudstone pressure. A key limitation of this approach was that it assumes that the mudstone permeability is homogenous and isotropic, despite the fact that there are large changes in vertical effective stress within these systems. Czerniak (2011) attempted to account for the permeability of the mudrock in these systems. They modified the average area approach presented by Flemings and Lupa (2004) to include a term that weighted the relative contribution of mudstone to sandstone pore pressure by the permeability within the mudstone and they interpreted that the mudstone permeability declined with increasing vertical effective stress in the reservoir. The result of their analysis is that the predicted pore pressure in the aquifer was lower than that predicted by the area method.

In this thesis, I explore the role of mudstone permeability on sandstone pressure. I show how mudstone permeability controls the pore pressure present in sandstone reservoirs and I develop a simple approach to predict the relationship between mudstone pressure and sandstone pressure. I then systematically study how mudstone permeability variation, stress conditions, reservoir structural relief, and lithological properties control fluid flow, and the reservoir overpressure. I verify our model by comparing it to basin modeling results and field pressure observations in the Bullwinkle Basin, Gulf of Mexico.

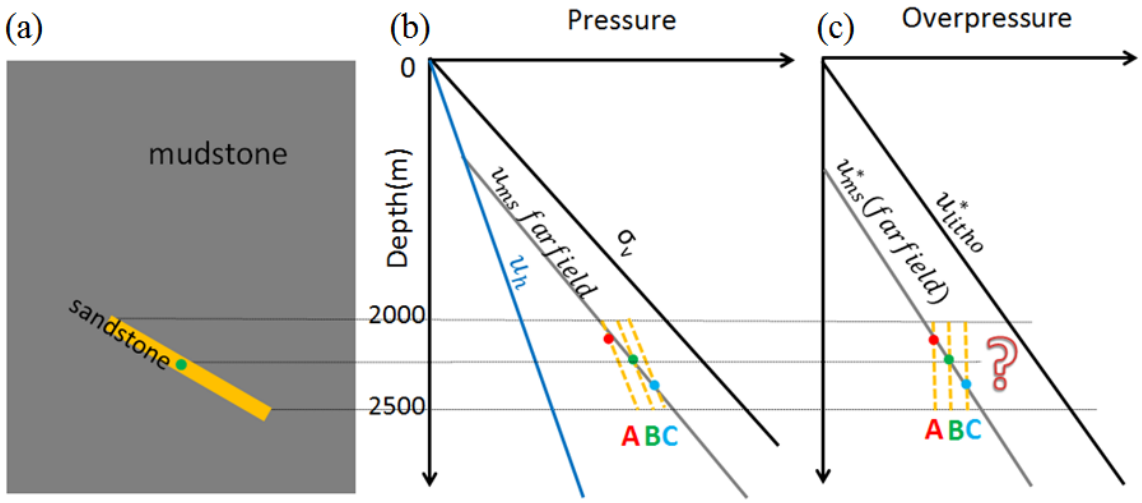

Figure 1.1: Sketch showing pressure system around a dipping reservoir

The meanings of the symbols are shown Table1
(a) A dipping sandstone reservoir is encased in mudstone. The crest of the reservoir is at 2000m and the base of the reservoir is at 2500m. The green point shows the mid-point of the dipping reservoir. (b) In the sandstone, the pressure gradient follows hydrostatic pressure gradient whereas the mudstone has a higher pressure gradient. A practical question is what the pore pressure is within the sandstone. (c) The corresponding overpressure plot.

Table 1.1: Nomenclature (Chapter 1)

Name	Description	Units
k	Intrinsic permeability	L^2
u	Pore pressure	M/LT^2
u^*	Overpressure	M/LT^2
u_h	Hydrostatic Pressure	M/LT^2
σ'	Vertical effective stress	M/LT^2
σ_v	Overburden stress	M/LT^2
σ_0'	Reference vertical effective stress	M/LT^2
θ	Angle of rotation	degree
mbsf	Meter below seafloor	L
ρ_b	Bulk density	M/L^3
e	Void ratio	Dimensionless
e_0	Reference void ration	Dimensionless
ϕ	Porosity	Dimensionless
ϕ_0	Reference porosity	Dimensionless
C_c	Compression index	Dimensionless
A_k	Coefficient for k model	$\log L^2$
B_k	Coefficient for k model	$\log L^2$
k_r	Permeability contrast ratio	Dimensionless
k_{crest}	Mudstone permeability at the crest	L^2
k_{base}	Mudstone permeability at the base	L^2
Z	Equal pressure depth parameter	Dimensionless
R	Structural relief	L

1.2 STATIC MODEL

I present a static modeling approach that uses the permeability variation in the mudstone to provide more accurate predictions for the depth where reservoir pressure equals mudstone pressure. I then use this model to systematically study the effects of farfield mudstone vertical effective stress, sandstone reservoir structural relief, and mudstone compressibility on the relationship between mudstone pressure and sandstone pressure.

1.2.1 Model Approach

I assume that pore pressure in the mudstone follows the lithostatic gradient whereas pore pressure in the reservoir follows the hydrostatic gradient. In the examples of this paper, the lithostatic gradient is assumed constant and equals to 22.6 MPa/km (1psi/ft) whereas the reservoir gradient is hydrostatic and equal to 10.3 MPa/km (0.46psi/ft). The reservoir has a total structural relief defined by the parameter *R*.

$$R = z_{base} - z_{crest} \quad (1.1)$$

where *R* is the reservoir relief, z_{base} is the deepest depth of the reservoir, and z_{crest} is the shallowest depth of the reservoir (True vertical depth subsea).

I assume that the fluid is incompressible, with constant viscosity, and flow is normal to the sand surface (**Fig. 1.2a**). Based on Darcy's law, the flux into the reservoir from the mudstone at any depth (i) is:

$$q_i = \frac{Q_i}{A_i} = \frac{-k_i}{\mu} \cdot \left(\frac{u^*_{res} - u^*_{ms}}{dx}\right), \quad (1.2)$$

where *k* is the intrinsic permeability of the mudstone near the reservoir at depth *z*, μ is fluid viscosity, A_i is area element normal to the reservoir surface, *dx* is the characteristic length scale of the flow, u_{ms}* is the mudstone overpressure, and u_{res}* is the reservoir overpressure.

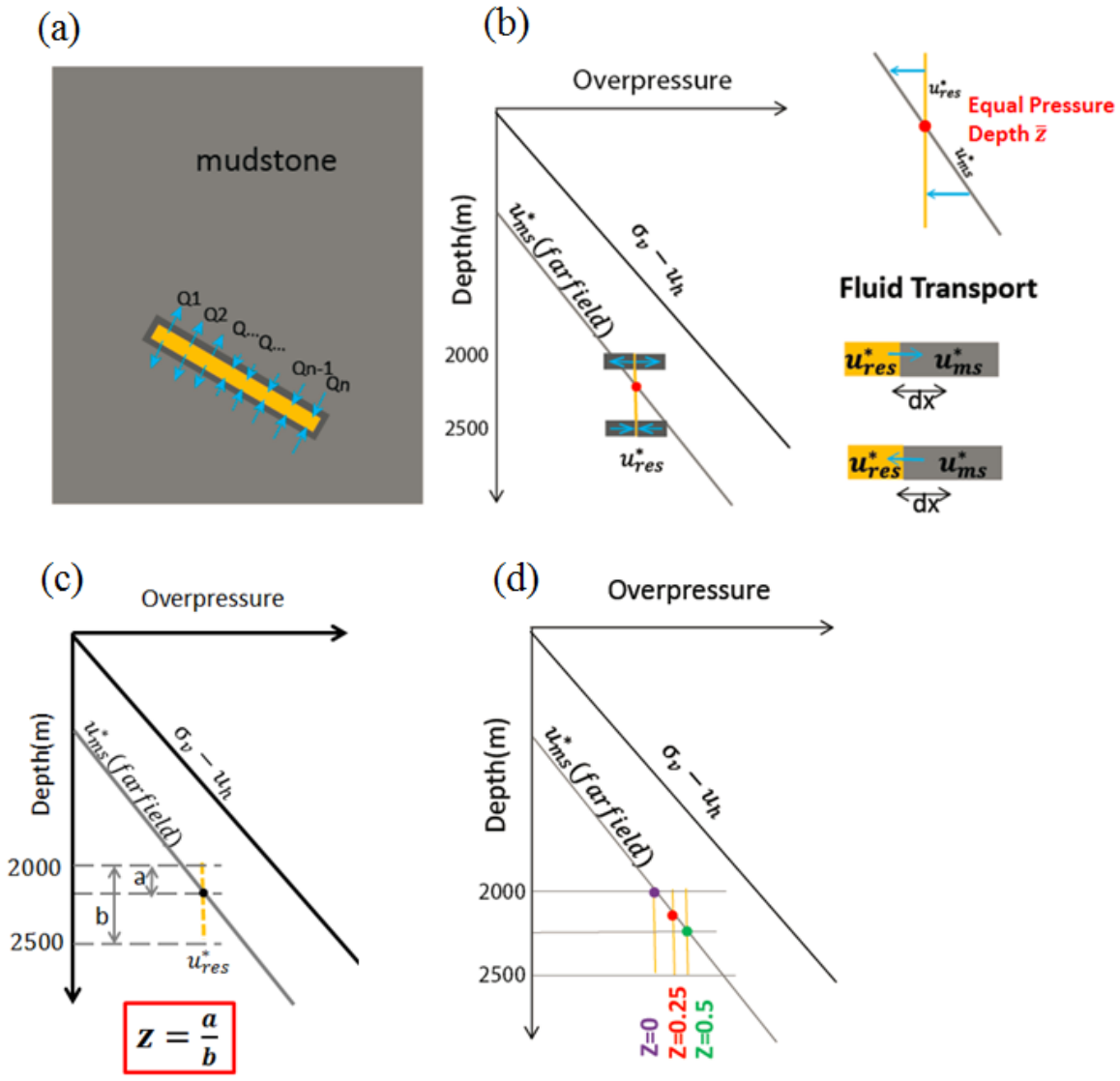

Figure 1.2: Static model and Z parameter

(a) A dipping reservoir encased in mudstone. (b) Above the depth where reservoir overpressure equals mudstone overpressure (equal pressure depth), fluid flows from the reservoir to the mudstone; below the equal pressure depth, fluid flows from the mudstone into the reservoir; (c) Definition of Z parameter; (d) The higher the Z value, the lower the equal pressure depth

For the system to be at steady state, the integral of the volume flux of the entire surface of the reservoir must be equal to zero:

$$Q = \iint_A \boldsymbol{q} \cdot \boldsymbol{n} \cdot dA = \iint_A \frac{-k_i(z)}{\mu} \cdot \left(\frac{u^*_{res} - u^*_{ms}}{dx}\right) \cdot \boldsymbol{n} \cdot dA = 0 \quad (1.3)$$

I assume the flow through the two ends (left and right) of the reservoir is negligible compared to the flow through to the top and bottom of the reservoir. In addition, flow through the top and bottom of the reservoir is assumed to be the same. Thus, for a two dimensional system of constant viscosity, this equation simplifies to **(Appendix A):**

$$\int_{z_{base}}^{z_{crest}} -k_i(z) \cdot (u^*_{res} - u^*_{ms}) \cdot dz = 0 \quad (1.4)$$

I integrate Equation 1.4 and solve for the value of u^*_{res} (**Appendix A)**. I introduce parameter Z (Flemings et al., 2002) to quantitatively describe the depth where the mudstone pressure equals the reservoir pressure: Z is the ratio of the distance between the crest depth and the depth where the reservoir pressure equals mudstone pressure divided by the total structural relief of the reservoir (**Fig. 1.2c**):

$$Z = \frac{\bar{z} - z_{crest}}{R} \quad (1.5)$$

where $\bar{z}$ is the depth where mudstone pressure equals reservoir pressure, *R* is the total structural relief, and z_{crest} is the shallowest depth of the structure.

The *Z* parameter shows the percentage of the structural relief that is above the depth where the sandstone and mudstone pressure are equal. Thus, $Z = 0$ means the reservoir pressure equals the mudstone pressure at the crest of the structure whereas Z=0.5 means that the pressures are equal at the midpoint of the structure (**Fig. 1.2d**).

If mudstone permeability *k* does not change and mudstone pressure has linear relationship with depth, integrating of Eq. 1.4 yields $Z = 0.5$. (**Appendix B**)

1.2.2 Example Case

I first present a simple example. The reservoir has a crestal height of 2000 mbsf (z_{crest} = 2000 m) and a basal height of 2500 m (z_{base}= 2500) (**Fig. 1.3a**). The water depth is assumed to be 0m. The overburden gradient is assumed to equal 22.6 MPa/km (1psi/ft). The hydrostatic pressure is assumed to equal 10.3 MPa/km (0.46psi/ft). The reduced lithostatic gradient is 12.3MPa/km, which is the lithostatic pressure less the hydrostatic pressure (black line, Fig. **1.3a**). The overpressure in the farfield mudstone is assumed to follow the reduced lithostatic gradient and be equal to 19.6MPa at z = 2000m (light grey line, Fig. **1.3a**). The farfield mudstone vertical effective stress is 5Mpa, which is the difference between the farfield mudstone overpressure and the reduced lithostatic pressure (Fig. **1.3a)**.

Finally, I need to define the permeability of the mudstone as a function of the vertical effective stress in the system. I use the experimental results of Constant-Rate-of-Strain tests to define the compression and permeability behavior of the mudstone. The samples are from Eugene Island, Gulf of Mexico and have mass of clay fraction of 65% (Betts, 2013 Thesis). The vertical effective stress, permeability, and porosity relationships of the mudstone are shown in **Fig. 1.4**. The detailed mathematical description is shown in **Appendix A**.

The solution to **Eq. 1.3** based on these parameters is that the equal pressure depth is at 2150m (**Fig. 1.3a**, $u^*_{res} = 21.5MPa$) and as a result the Z value is 0.31.

The Z value is 0.31 as opposed to 0.5 in the case where permeability does not change because the permeability of the mudstone declines with depth (**Fig1.3b**). As the vertical effective stress increases from about 3MPa to 9MPa, the mudstone is compressed continuously, and the permeability of the mudstone surrounding the reservoir decreases

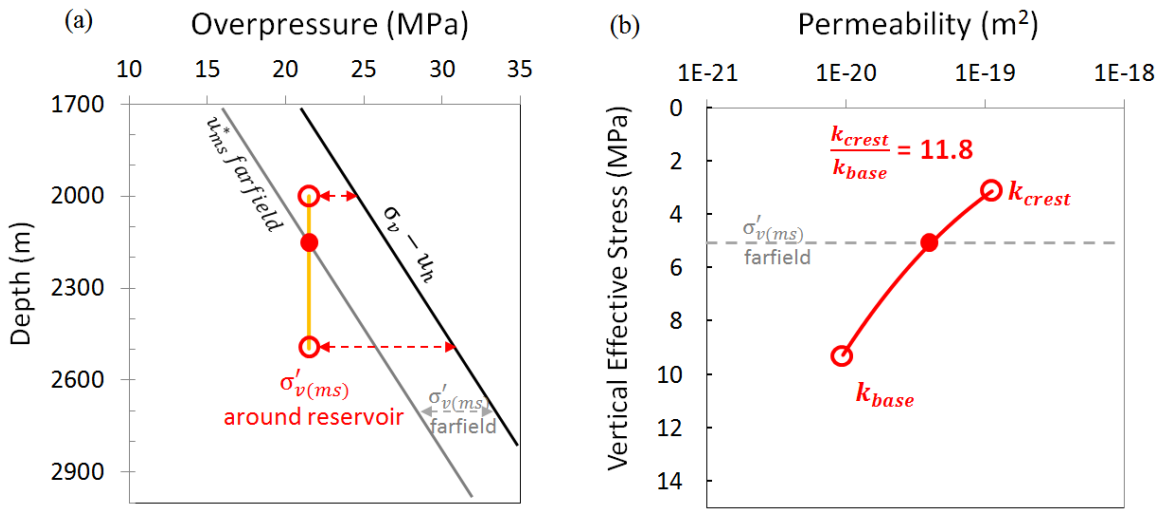

Figure 1.3: Example Case

(a) Overpressure plot. Round circles show the crest and bottom depths of the reservoir structure. The black line indicates the reduced lithostatic pressure. Grey line shows the overpressure in the farfield. The red dot shows the calculated equal pressure depth. (b) Permeability plot. Around the dipping reservoir, the permeability in the mudstone decreases by about a factor of 11.8 from the crest to the base of the reservoir. The grey dash line shows the farfield mudstone vertical effective stress (5MPa). The mudstone permeability in the farfield is about 4E-20m^2.

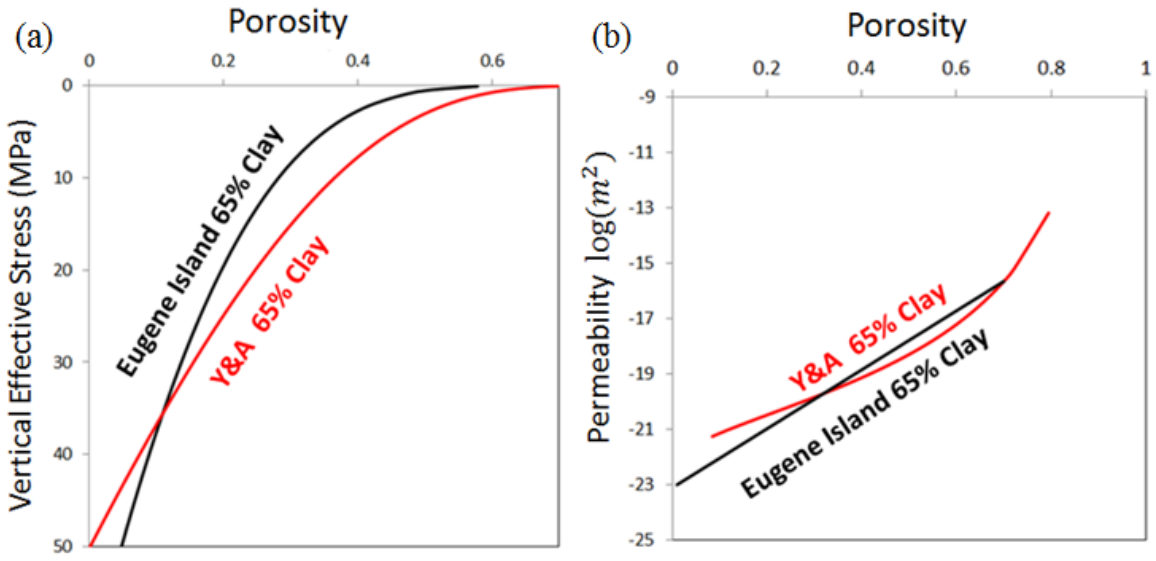

Figure 1.4: Lithological properties

(a) Compression model of Eugene Island mudstone with 65% clay fraction (black) and that of Yang and Aplin mudstone with 65% clay fraction (red). (b) Permeability model of Eugene Island mudstone with 65% clay fraction (black) and that of Yang and Aplin mudstone with 65% clay fraction.

from the crest location (1.1E-19m^2) to the base location (9.5E-21m^2) (**Fig. 1.3b**). From the crest to the base, the permeability of the mudstone decreases by about 11.8 times. To describe the degree of permeability contrast, I introduce parameter k_r, which is the ratio of mudstone permeability close to the crest of the reservoir to the permeability of the mudstone close to the base of the reservoir. In this case, $k_r = \frac{k_{crest}}{k_{base}} = 11.8$.

1.2.3 Effects of farfield mudstone vertical effective stress and structural relief

I next discuss the effect of farfield mudstone vertical effective stress on the relationship of mudstone and sandstone overpressure, and then I discuss the effect of the sandstone's structural relief.

1.2.3.1 Effect of farfield mudstone vertical effective stress

Now consider a case with the same structural relief (500m), but a higher farfield mudstone vertical effective stress, $\sigma'_{v(ms)}$ farfield = 20MPa (**Fig.1.5a**). The mudstone overpressure gradient still follows the reduced lithostatic pressure gradient and it equals 4.6MPa at z = 2000m.

The result of this example is that the equal pressure depth is at 2210m (green symbol, **Fig. 1.5a).** The predicted reservoir overpressure $u^*_{res} = 7.2MPa$ and Z value equals 0.42 (**Fig. 1.5c**). The Z value 0.42, obtained from this high mudstone vertical effective stress example, which is greater than the previous example, is caused by a low permeability contrast k_r. Under the higher effective stress conditions, there is less change in mudstone permeability than under low stress conditions. In the example, with high farfield mudstone vertical effective stress, the mudstone vertical effective stress increases from 17.4Mpa to 23.6Mpa and the mudstone permeability decreases from 1.5E-21m^2 to 5.4E-22m^2 along the dipping reservoir. The mudstone permeability contrast k_r = 2.8 (**Fig. 1.5b**). Compare the high farfield mudstone vertical effective stress example and low

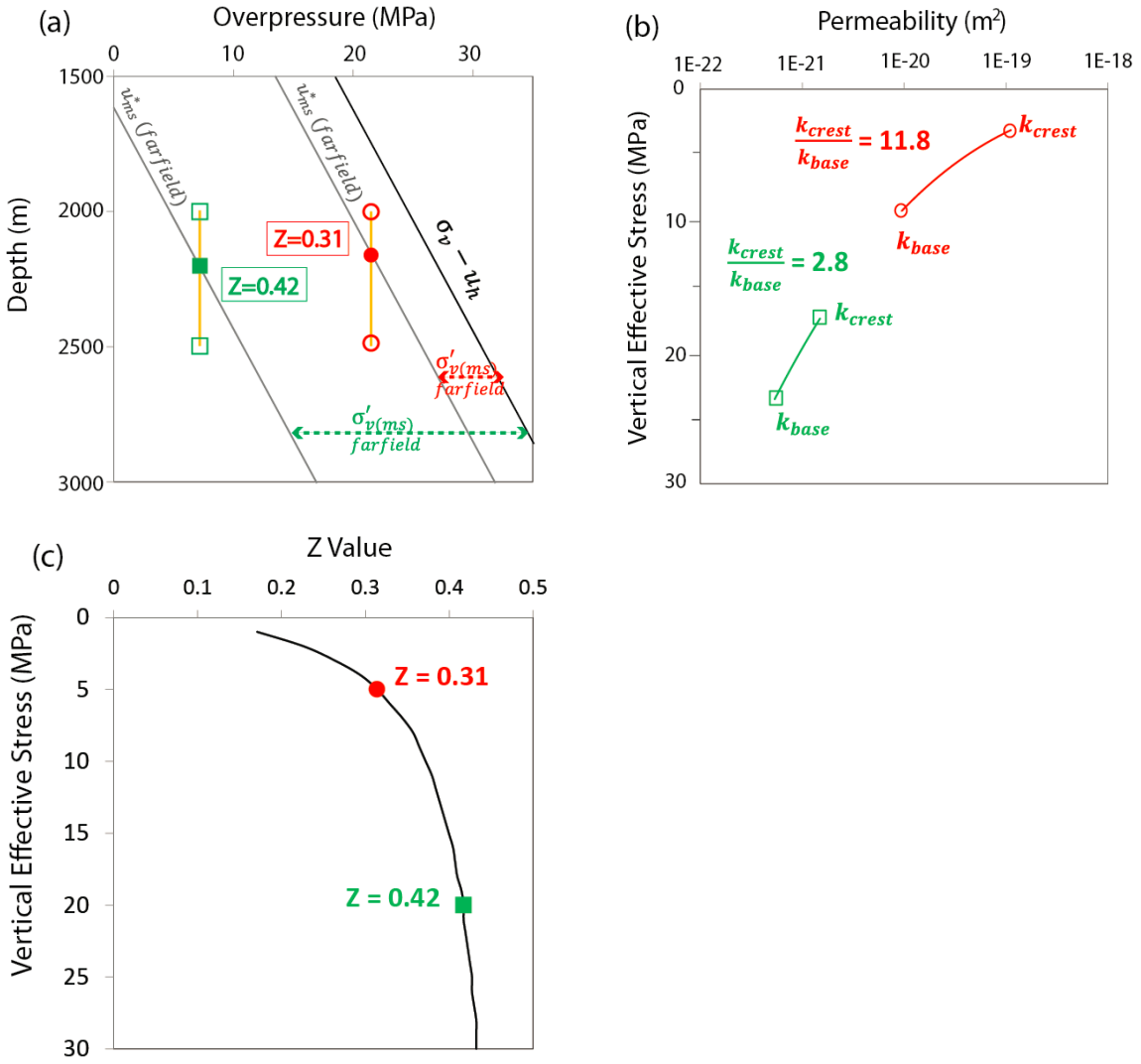

Figure 1.5: Effect of vertical effective stress level on permeability changes and the equal pressure depth

(a) Overpressure plot. Lower farfield overpressure (hence higher farfield vertical effective stress (green line)) leads to a greater equal pressure depth compared to higher farfield overpressure (lower farfield vertical effective stress (red line)). (b) Permeability versus vertical effective stress plot. The higher farfield vertical effective stress (green), leads to a much smaller permeability decrease around the reservoir than the lower farfield vertical effective stress, (factor of 2.8 vs. 11.8 respectively). (c) Location of the Z parameter. The higher the farfield vertical effective stress, the higher the Z value and hence, the greater the equal pressure depth.

farfield mudstone vertical effective stress example (**Fig. 1.5b**); the low farfield vertical effective stress case (with red circle symbols) has a higher permeability contrast (k_r =11.8) than that of the high farfield vertical effective stress example (k_r =2.8, with green square symbols).

Thus, for the same structural relief, the higher the farfield mudstone vertical effective stress leads to (1) the less mudstone permeability contrast surrounding the reservoir, (2) a higher Z value and (3) a greater equal pressure depth.

1.2.3.2 Effect of sandstone structural relief

I next explore the effect of structural relief by considering a case where the structural relief (R) is 1500 m in contrast to the last example where it was 500 meters. The farfield mudstone vertical effective stress $\sigma'_{v(ms)}$ farfield equals 5Mpa (the same as that in **section 1.2.2**).

The result of this case is that the equal pressure depth is at 2225m ($u^*_{res} = 22.4MPa$) and the Z parameter value equals 0.15 (**Fig. 1.6c**). The low Z value 0.15 obtained from this high structural relief example is due to a greater permeability contrast k_r. In this 1500m structural relief example (**Fig.1.6**, with blue triangles), along the dipping reservoir, the mudstone vertical effective stress increases from 2.3MPa to 20.8MPa and the mudstone permeability decreases from 2.0E-19m^2 to 8.4E-22m^2 **(Fig.1.6b).** This dramatically mudstone permeability change yields the permeability contrast parameter k_r = 233.5. On the contrary, in the low structural relief example (red line, **Fig.1.6b**), the mudstone undergoes much less vertical effective stress and permeability change, which results in a permeability contrast parameter k_r = 11.8.

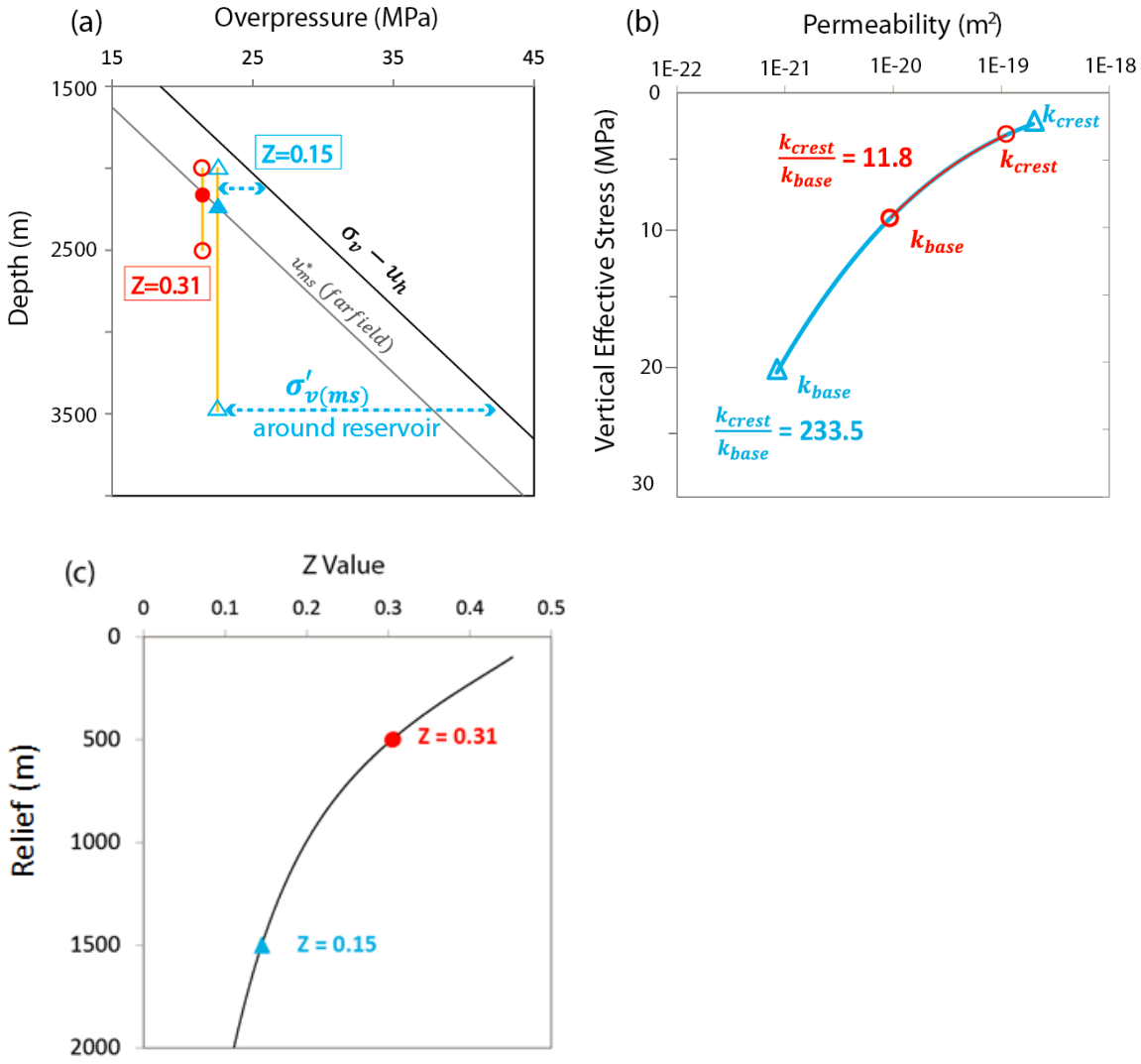

Figure 1.6: Effect of structural relief on permeability changes and the equal pressure depth

(a) Overpressure plot. The higher the structural relief, the shallower the equal pressure depth (b) Permeability versus vertical effective stress plot. The permeability change around the reservoir increases dramatically with the increase in the structural relief (k_r=233.5). (c) Z parameter versus reservoir structural relief. The higher the structural relief, the lower the Z value and so the shallower the equal pressure depth.

This comparison shows that if the farfield mudstone vertical effective stress remains the same, then, higher structural relief leads to (1) the higher mudstone vertical effective stress change near the reservoir, (2) higher mudstone permeability contrast along the dipping reservoir, (3) a lower the Z value, and the shallower equal pressure depth.

1.2.3.3 Z value Nomogram

I summarize the effect of reservoir structural relief and farfield mudstone vertical effective stress on the *Z* value, the parameter indicates the equal pressure depth (**Fig. 1.7**). As relief increases, the *Z* value decreases and the equal pressure depth shifts towards the crest. As the farfield vertical effective stress increases, the *Z* parameter increases, which indicates that the equal pressure depth is close to the mid-point of the structure.

1.2.4 Effect of mudstone compressibility

In this section, I study the effect of mudstone compressibility on the depth where reservoir overpressure equals farfield mudstone overpressure. I first introduce the compression index, C_c, which can be mathematically described as follows:

$$C_c = \frac{e_1 - e_2}{log(\frac{\sigma_2'}{\sigma_1'})} \quad (1.4)$$

where e_2 and e_1 are the mudstone void ratio at the vertical effective stress of σ_2' and σ_1' respectfully.

The rock with a higher C_c value has a higher compressibility and vice versa. **Fig. 1.8a** show two mudstone compression curves: one with high compressibility, C_c=0.49 (the same as that I used in **section 1.2.2**) and the second one with low compressibility, C_c = 0.2.

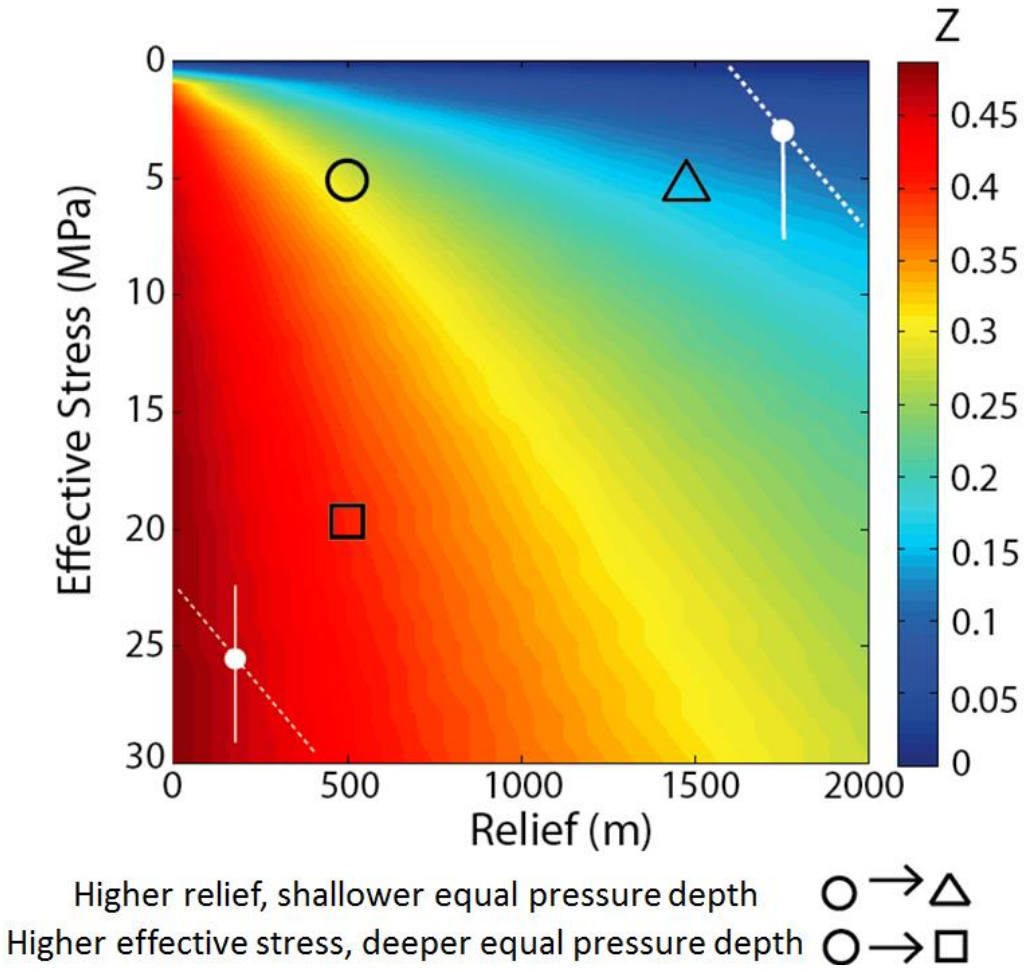

Figure 1.7: Equal pressure depth nomogram

Location of the Z parameter as a function of the reservoir structural relief and the farfield vertical effective stress. Warmer colors indicate a higher Z value and greater equal pressure depth, and vice versa. The circle marker shows that for the case with 500m relief and 5MPa farfield vertical effective stress, the equal pressure depth is at about 1/3 of the reservoir structure (Z= 0.31). The triangle shows that for the case with 1500m relief and 5MPa farfield vertical effective stress, the equal pressure depth is at a depth of about 1/7 of the reservoir structure (Z= 0.15). The square marker shows that for the case with 1500m relief and 20MPa farfield mudstone vertical effective stress, the equal pressure depth is at a depth of 2/5 of the reservoir structure (Z= 0.43).

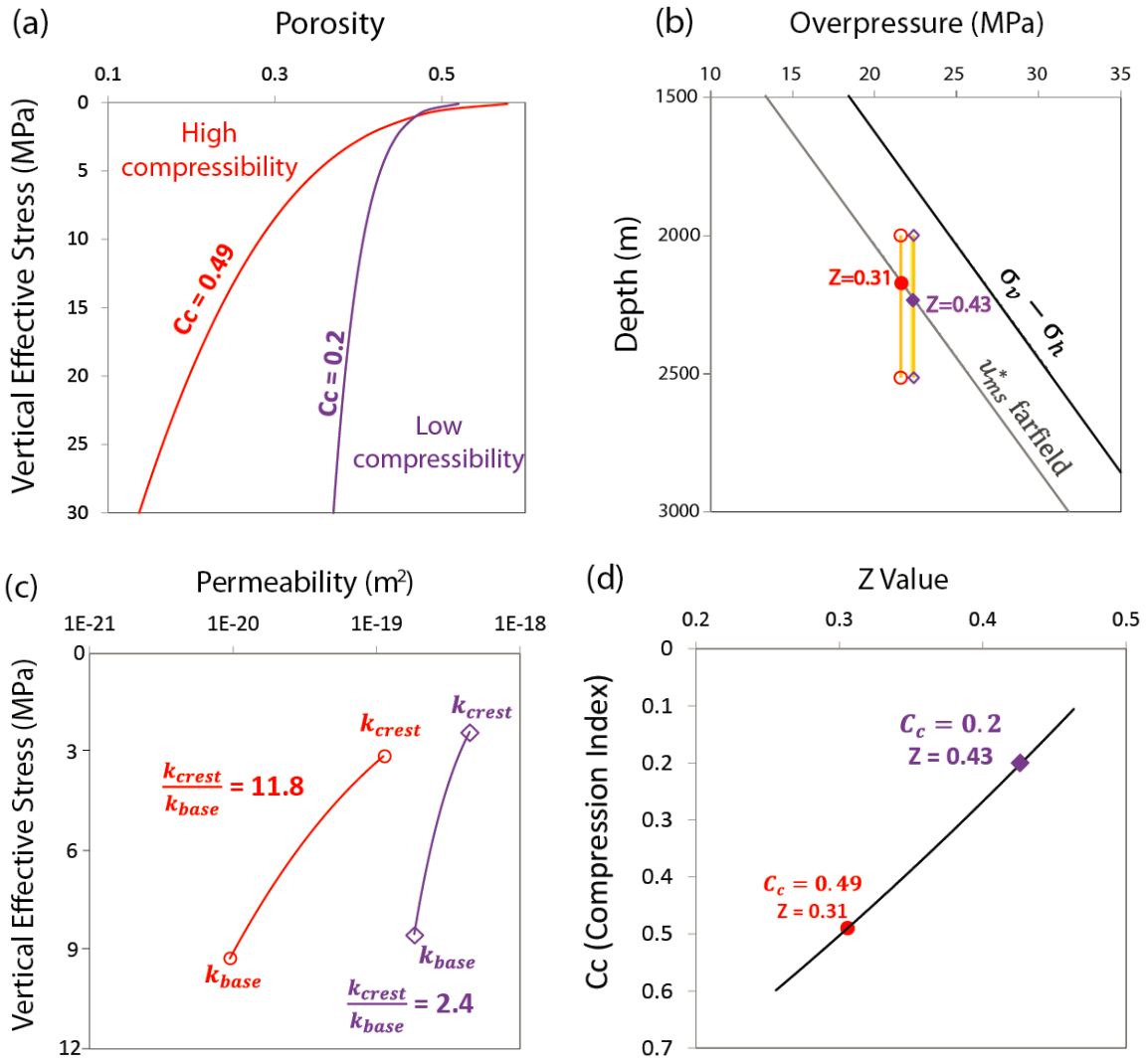

Figure 1.8: Effect of compressibility on permeability changes and the equal pressure depth

(a) Uniaxial compression behavior for 2 compressibility values (C_C = 0.2 (purple) and 0.49 (red)). (b) Overpressure plot. The higher mudstone compressibility leads to a shallower equal pressure depth (c) Permeability versus vertical effective stress plot. Increasing compressibility leads to a larger change in the permeability in the mudstones around the reservoir. (d) Parameter Z versus compressibility. The higher the compressibility (Cc), the lower the Z value, and hence, the shallower the equal pressure depth.

The results of the low compressibility example (C_c = 0.2) is that the equal pressure depth is at z = 2215m. Z parameter equals 0.43 and the predicted reservoir overpressure $u^*_{res} = 22.2Mpa$.

The high Z value 0.43 from the low mudstone compressibility example is due to the low permeability contrast. In the low mudstone compressibility example (**Fig. 1.8**, with purple symbols), as the mudstone vertical effective stress increases from about 2.4Mpa to 8.5Mpa (**Fig. 1.8c)**, the mudstone permeability decreases from about 4.5E-19m^2 to 1.8E-19m^2 along the crest to the base of the reservoir. The permeability contrast k_r is 2.4 in the low mudstone compressibility example. In the high mudstone compressibility case, even though the mudstone vertical effective stress change is similar (increase from about 3Mpa to 9Mpa), the mudstone permeability change is much greater (k_r=11.8) (**Fig. 1.8c).**

Thus, lower mudstone compressibility leads to: (1) lower mudstone permeability contrast, (2) higher Z parameter, (3) greater depth where reservoir overpressure equals mudstone overpressure.

1.2.5 Comparison with other mudstone models

We commonly use various lithology models for different study regions. In this section, I use Yang and Aplin's (2004, 2010) model as a comparison example to study how the lithology models affect the relationship of sandstone and mudstone overpressure. **Figure1.4** (red lines) shows the permeability and compression behaviors of the mudstone with clay fraction of 65% (Yang and Aplin, 2004, 2010). **Figure 1.9** shows the relative difference of Z parameter predicted by using Eugene Island's lithology model (65% clay) and Yang and Aplin's lithology model (65% clay).

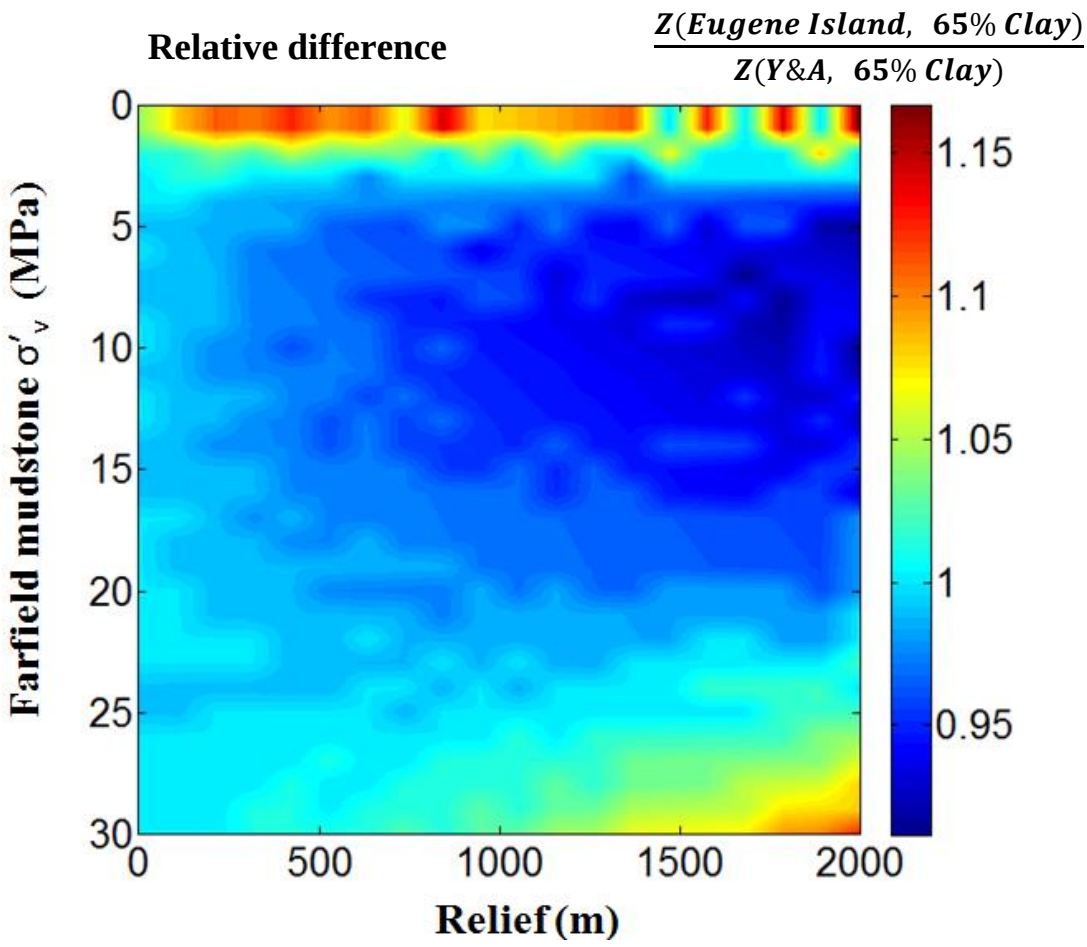

Figure 1.9: Effect of lithology on the Z parameter

I compare 2 mudstones with the same clay content (65%) but different lithology model (Eugene Island and Y&A((Yang and Aplin, 2004, 2010). *The different lithology doesn't not have much effect on the equal pressure depth (with the exception of low vertical effective stress levels).*

The relative difference in Z is small by using these two lithology models, which indicates the depth where reservoir pressure equals farfield mudstone pressure is not very sensitive to a particular mudstone model.

1.3 Model Verification and Validation

To test the reliability of the static model, I compare the static model results to both the basin model results and field pressure observations.

1.3.1 Basin Model

To study the effect of spatial permeability variations on overpressure development, I use a forward model approach (basin model) that couples sedimentation and flow behavior during burial. The control equation is shown in **Eq1.5** (Hantschel and Kauerauf, 2009):

$$\frac{\partial u}{\partial t} = \nabla \cdot \left(\frac{1-\phi}{C} \cdot \frac{k}{\mu}\right) \cdot \nabla u + \frac{\partial \sigma_v}{\partial t} \qquad (1.5)$$

Where, u is pore pressure, t is time, ϕ is porosity, k is intrinsic permeability, σ_v is lithostatic pressure, μ is viscosity, and C is compressibility. The equation shows that pore pressure changes during burial are related to both rock mechanical properties and the sediment loading rate. To compare permeability variation in the mudstone around the dipping reservoir and its effect on the depth where reservoir pressure equals mudstone pressure, I construct two basin models: a constant permeability model and C a porosity dependent permeability model. First, I set up the model frame.

1.3.1.1 Model frame set-up and boundary conditions

I model the burial and consolidation of a sandstone reservoir (**Fig. 1.10**). First, a 20km thick layer is deposited between 0m.y. and 20m.y.. Second, a 0.3km thick, 6km long sandstone was deposited on top of the previous mudstone layer between 20 m.y. and 23m.y.. Mudstone was deposited laterally to the sandstone. Finally, another mudstone

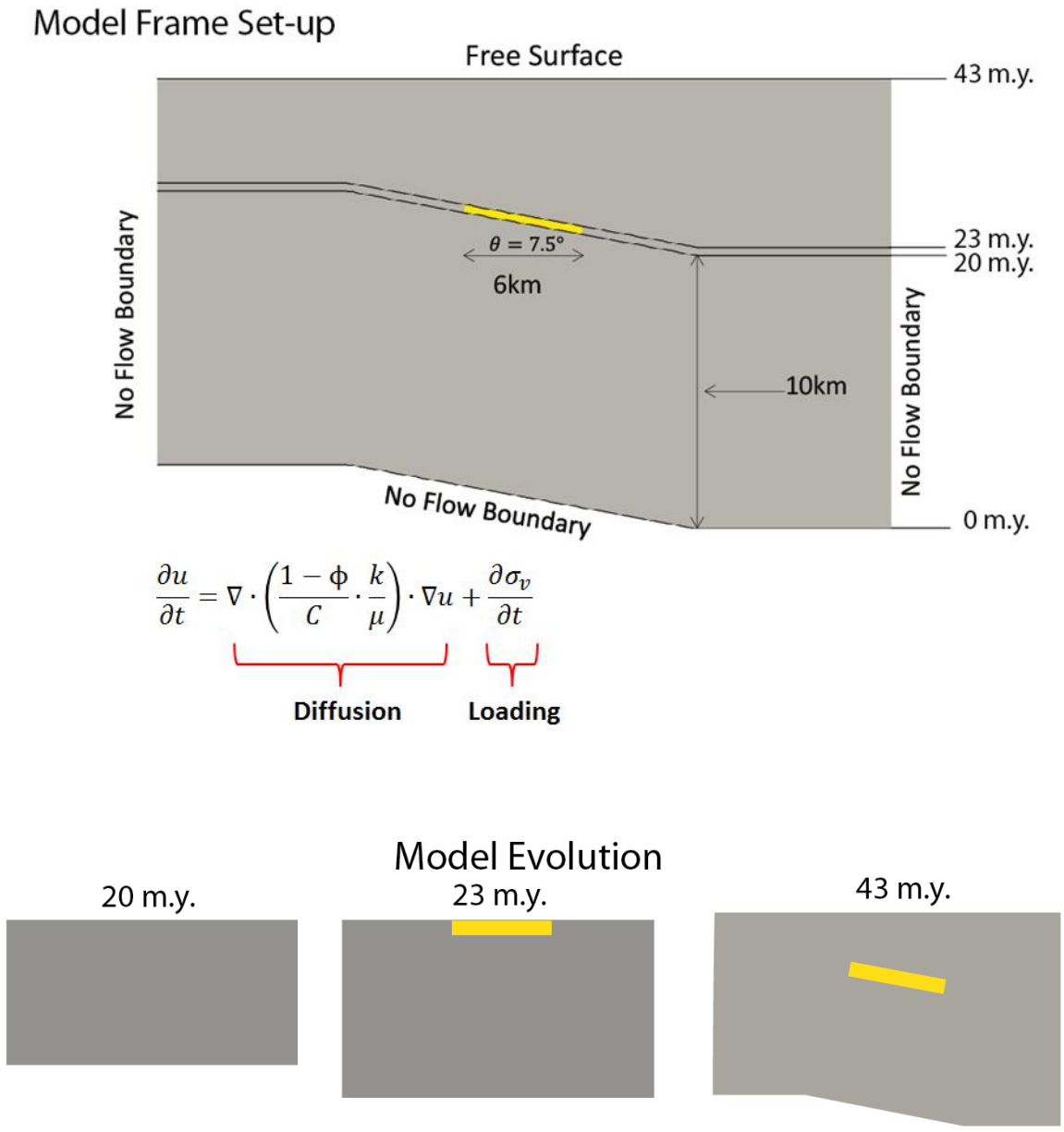

Figure 1.10: Basin model frame set-up

A 10km thick mudstone was deposited from 0m.y. to 20m.y.. A sandstone layer about 300m thick and 6km long (bounded with mudstone at both sides) was deposited from 20m.y. to 20m.y.. The mudstone was buried and tilted by the overlying mudstone. The sea floor is a free surface boundary whereas the sides are no flow boundaries.

layer was deposited asymmetrically on top of the sandstone layer between 23m.y. and 43m.y.. The left end of the sandstone was buried to a depth of 4780m depth and the right end was buried to 5570m. The angle of the dipping sand reservoir is about 7.5 degrees. The water level, which is assumed to lie at the upper sediment surface, does not change with time. In this basin model, no overpressure is generated at the seafloor. The left, right, and bottom sides are no-flow boundaries.

1.3.1.2 Lithological properties

Sandstone and mudstone compressibility and permeability are described in this section. For the compressional behavior of the mudstone and sandstone, I assume that the void ratio is proportional to the log of vertical effective stress as in **Eq. 1.6** (**Fig.11a**).

$$e = e_0 - C_c log(\frac{\sigma'}{\sigma_0'}) \qquad (1.6)$$

where e is the void ratio, which is proportional to porosity;

$$e = \frac{\phi}{1-\phi} \qquad (1.7)$$

e_o is the reference void ratio, the void ratio present at a reference vertical effective stress (σ_0') of 1MPa, and C_c is the compression coefficient of primary consolidation.

The specific compression parameters used for this simulation are shown in **Table1.2**. The parameters for mudstone compression model are from CRS test and the test samples are from Eugene Island, Gulf of Mexico (Betts, 2013). The parameters for sandstone compression are from the lab tests on the samples from Green Canyon Block 65, Gulf of Mexico (Kevin, 2002). **Eq. 1.6** has been used in soil mechanics for decades(Dugan et al., 2003; Lambe and Whitman, 1979; Terzaghi et al., 1996) and has also been applied to describe the compression behavior of geological systems (Dugan et al., 2003; Long et al., 2011; Saffer, 2003; Schneider et al., 2009; Stigall and Dugan, 2010)

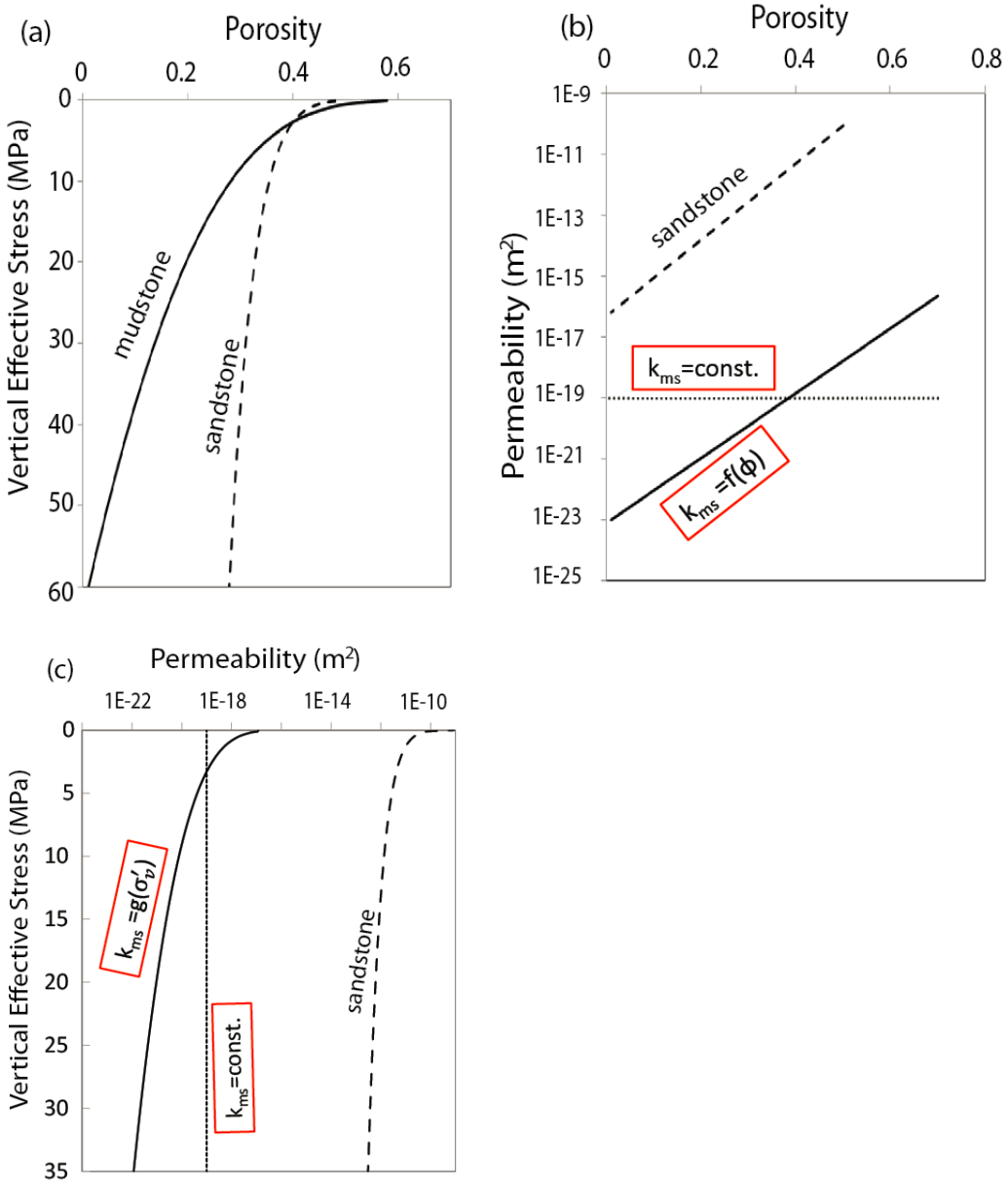

Figure 1.11: Lithology properties of basin models

(a) Compression behavior of the sandstone and mudstone in the basin model. (b) Permeability as a function of porosity for the constant permeability mudstone (dotted line), the variable permeability mudstone (solid line) and the sandstone (dashed line). (c) Permeability is a function of effective stress (combine (a) and (b)).

Table 1.2: Lithology Parameters

Lithology	e_0	σ_0' (MPa)	C_c	A_k (log(m^2))	B_k (log(m^2))
Sandstone	0.76	1	0.21	12.5	-16.3
Mudstone (Various Perm)	0.88	1	0.49	10.65	-23.1
Mudstone (Const. Perm)	0.88	1	0.49	0	-19

The parameters of the sandstone properties are from the sample in Green Canyon Block 65, GOM. The parameters of the mudstone properties are from the sample in Eugene Island, GOM.

I use two approaches to model mudstone permeability (**Fig.1.11b**). In the constant permeability model, mudstone permeability is assumed to be constant (1.0E-19m^2). In the porosity dependent permeability model, I assume a log linear relationship between permeability and porosity in the mudstone (**Table 1.2, Fig 1.11)**:

$$log(k) = A_k\phi + B_k \quad (1.8)$$

where A_k and B_k are empirical constants (Mello et al., 1994), which can be measured from the constant rate of strain consolidation (CRS) tests. The permeability model for the porosity dependent permeability model (Various Perm) is based on the CRS test results (Eugene Island sample, (Betts, 2013)). The sandstone permeability model is based on the lab test of sandstone samples from Green Canyon Block 65, Gulf of Mexico (Kevin, 2002).

1.3.1.3 Basin model results

1.3.1.3.1 Constant permeability

In this model, mudstone permeability is constant (1.0E-19m^2) during burial. The equal pressure depth is at the midpoint of the structure (about 5160m, **Fig. 1.12**) and it results in Z parameter equals 0.5. This result is consistent with the previous analysis: when the mudstone permeability is assumed constant, the equal pressure depth is at the midpoint of the structure.

1.3.1.3.2 Variable permeability

The reservoir overpressure predicted by the basin model (variable mudstone permeability) equal the farfield mudstone overpressure at 4870m and the reservoir overpressure is predicted to be about 41.2Mpa and the Z parameter equals 0.27.

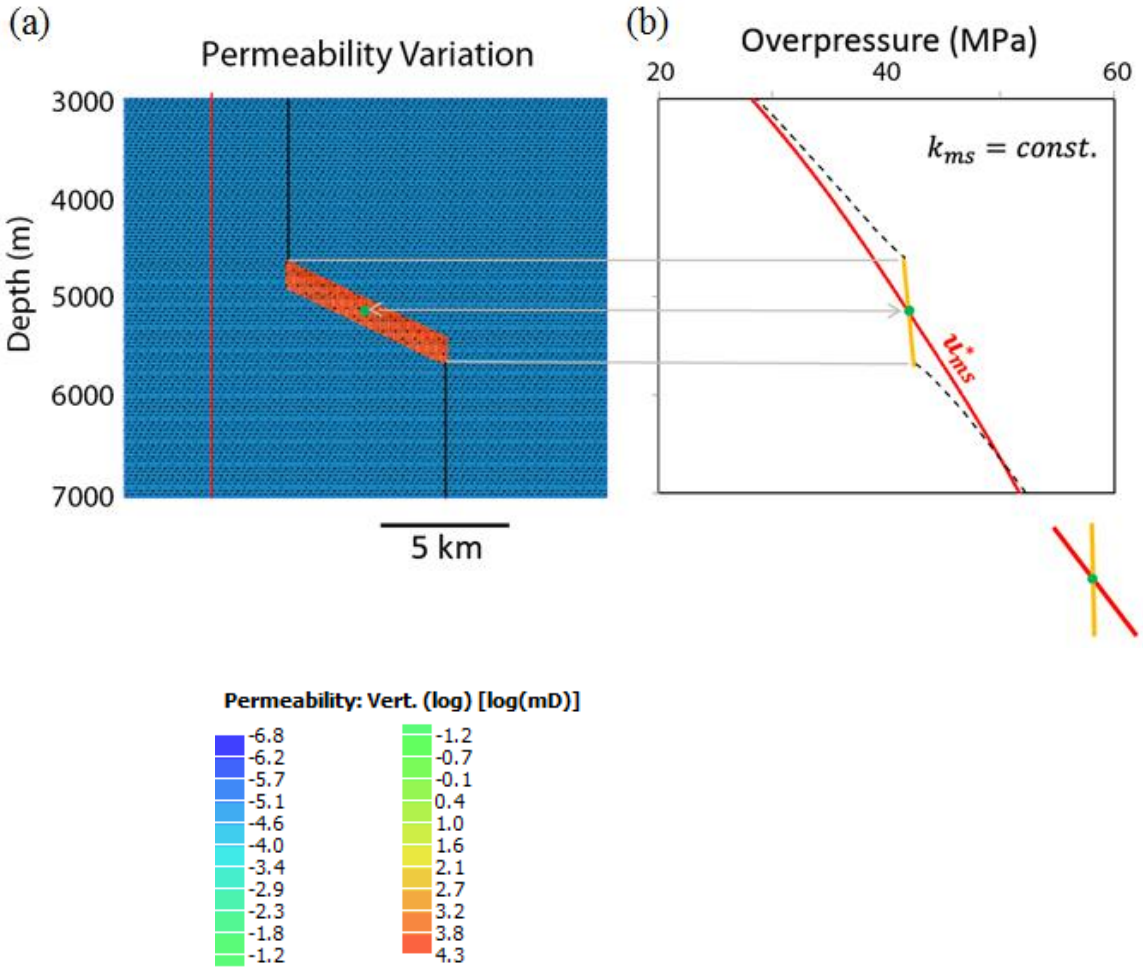

Figure 1.12: Basin model (constant permeability)

(a) Permeability Variation. The mudstone permeability is kept constant.
(b) Overpressure plot. The equal pressure depth is at the midpoint of the structure.

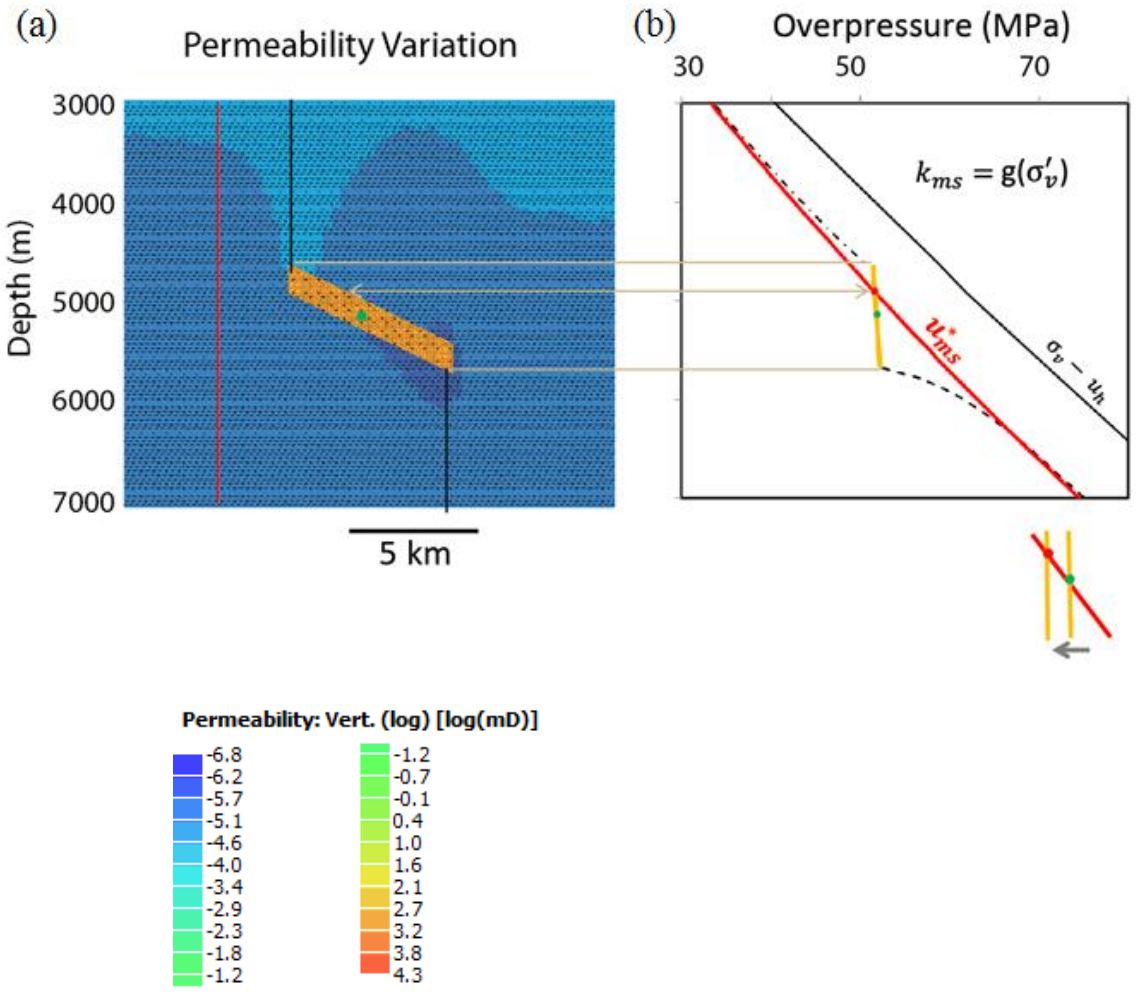

Figure 1.13: Basin model (variable permeability)

(*a) Permeability variation. Mudstone permeability is decreased (darker blue) around the base of the reservoir and increased (lighter blue) around the crest of the reservoir. (b) Overpressure Plot. The equal pressure depth is at ¼ depth of the reservoir relief.*

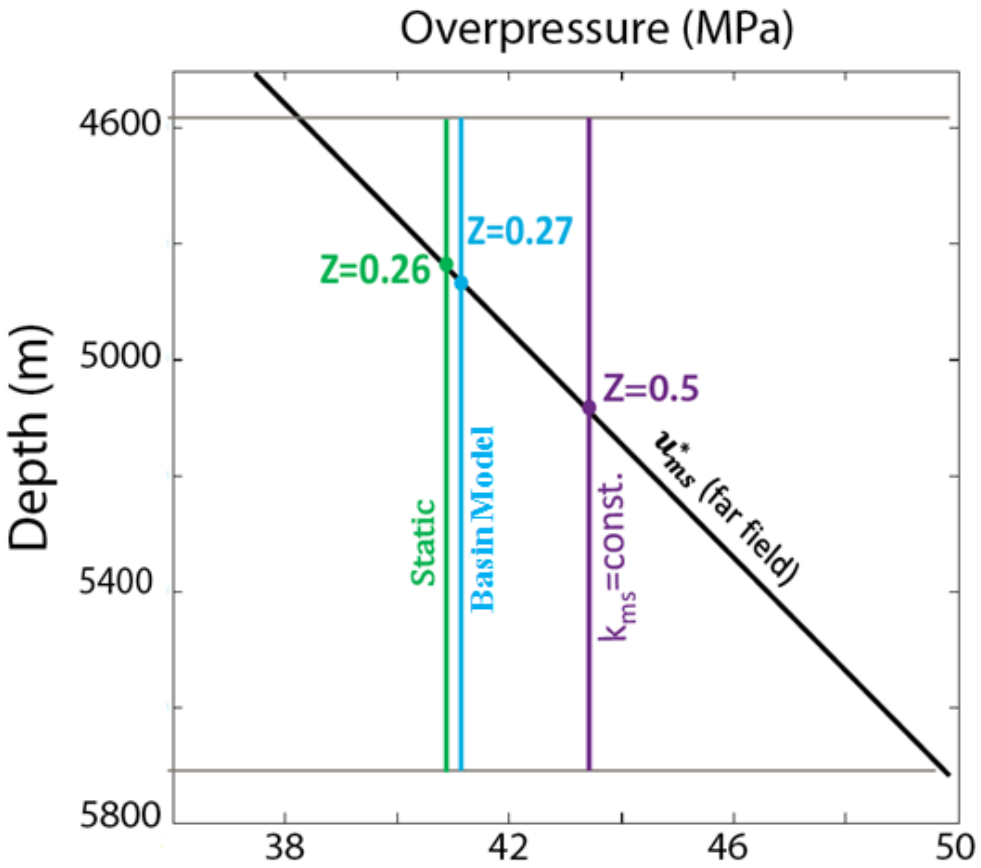

Figure 1.14: Model results comparison.

The basin model result (blue) is the one that from various permeability model (Fig.1.13). The Z parameter predicted from the basin model and static model are 0.27 and 0.26 respectfully.

The variable permeability model is more realistic because it accounts for changes in mudstone permeability during burial. At the far field, as sediments are deposited, existing sediments are buried, and hence vertical effective stress increases, and the porosity and permeability of the sedimentary package decreases. In addition, near the dipping structure, permeability also changes due to the local flow in and out of the reservoir. At the final stage (**Fig. 1.13**), mudstone permeability is lower around the base of the dipping reservoir and higher at the crest. The difference is approximately one order of magnitude in this case.

Using the information from the variable permeability basin model (relief R = 1100m, farfield mudstone vertical effective stress equals 10.5MPa, **Fig. 1.13**), I ran the static model and obtained parameter Z equals 0.26 and the depth where reservoir overpressure equals mudstone overpressure at about 4850m. The reservoir overpressure predicted by static model is about 41.1MPa. These results show that the overpressure pressure predicted from static model agrees with overpressure predicted from basin models.

1.3.1.4 Discussion of basin model results

These two basin model results prove that mudstone permeability around a dipping reservoir has a significant effect on the relationship of reservoir overpressure and mudstone overpressure. When the mudstone permeability is assumed constant, the depth where sandstone and mudstone pressure are equal is at the midpoint of the structure; however, when mudstone permeability is a function of vertical effective stress, the equal pressure depth is shallower. In terms of a physical explanation, I propose that as the fluid in the mudstone near the bottom of the reservoir is drained into the reservoir, the mudstone becomes more consolidated (has a higher vertical effective stress) than the

mudstone in the far field. The higher vertical effective stress leads to lower permeability around the down-dip portion of the reservoir. As a result, less high overpressure fluid in the deeper mudstone contributes to overpressure development inside the reservoir due to the low permeability. In other words, the reservoir is more isolated from the highly overpressured fluid. In contrast, the mudstone around the reservoir crest has a lower vertical effective stress, higher porosity, and higher permeability.

1.3.2 Compare field pressure observations in the Bullwinkle Basin, Gulf of Mexico

The Bullwinkle Basin is located offshore about 250 km southwest of New Orleans on the Gulf of Mexico continental slope (Flemings and Lupa, 2004). The field is in Green Canyon Block 65 in 1350 feet of water. Rapid sedimentation loading caused the salt underneath to withdraw and form the Bullwinkle Basin in Late Miocene to Early Pliocene slope (Flemings and Lupa, 2004).

The J sandstone package, which formed at 3.35Ma, hosts significant hydrocarbon reserves (Flemings and Lupa, 2004). The package is composed of amalgamated channels and turbidities. The depletion curves observed during production (Holman and Robertson, 1994) show that the sandstones are highly interconnected and not compartmentalized as often occurs with depositionally and structurally complex reservoirs such as these (Snedden et al. 2007).

I use the static model to predict overpressure in the J sand package. The crest of the J sand package is about 3300m and bottom is about 4060m. Therefore, the relief of the J sand package is about 760m. Farfield mudstone overpressure was estimated from the sonic logging data (Flemings and Lupa, 2004). Using the lithostatic pressure and estimated farfield mudstone overpressure, the farfield mudstone vertical effective stress is

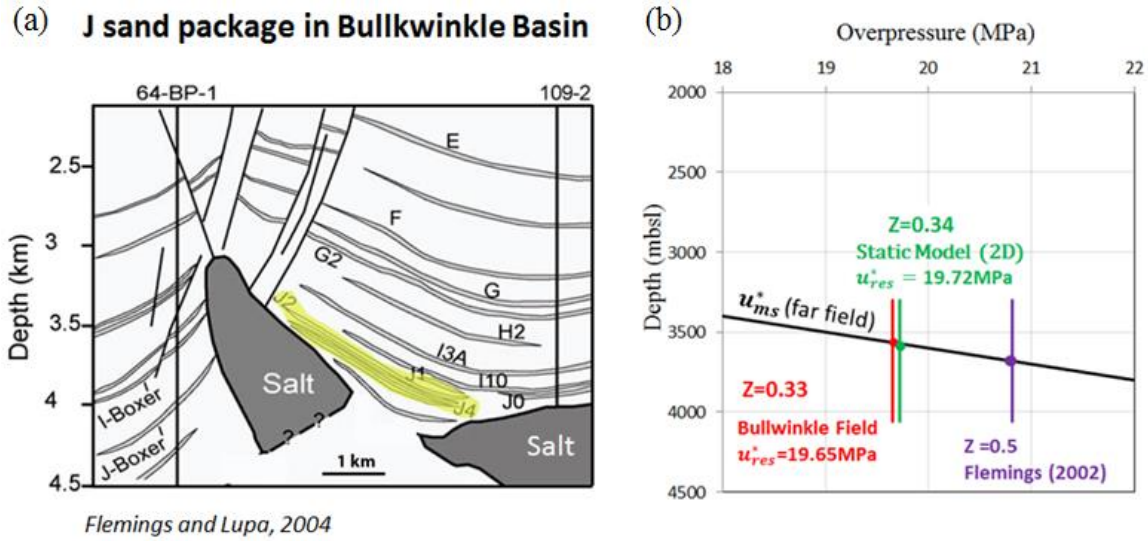

Figure 1.15: Comparison with field observations.

(a) Cross section of the Bullwinkle mini basin, showing the J sand reservoir (yellow).
(b) The static model closely predicts the field pressure observation.

calculated to be about 13MPa. Using the nomogram that I generated in **Fig.1.7**, the static model results indicate that the Z parameter is approximately 0.34. The reservoir overpressure is predicted to be 19.72MPa. Compared to the field pressure observation (Z=0.33, 19.65MPa), the static model results agree relatively closely with field pressure observations (**Fig. 1.15**).

1.4 DISCUSSION

Based on the flow balance concept, reservoir overpressure is determined by both mudstone permeability and mudstone overpressure. **Eq.1.4** can be re-written in is integral form:

$$u_{res}^{*} = \frac{\int_{z_1}^{z_2} k_{ms} \cdot u_{ms}^{*} \cdot dz}{\int_{z_1}^{z_2} k_{ms} \cdot dz} \quad (1.9)$$

Overpressure in the mudstone surrounding the reservoir differs from overpressure in the farfield mudstone. The overpressure gradient of the farfield mudstone is usually parallel to the reduced lithostatic pressure gradient. However, in proximity to a high permeability reservoir, the mudstone connected to the reservoir no longer follows the reduced lithostatic pressure gradient. The mudstone connected to the reservoir follows the reservoir overpressure. As the distance between the mudstone and reservoir increases, the reservoir effect diminished and the mudstone overpressure gradient gradually falls back to follow the reduced lithostatic pressure gradient.

A characteristic mudstone permeability variation exists around a dipping reservoir: mudstone permeability is lower near the base of the reservoir and higher near the crest of the reservoir. Near the reservoir base, the fluid drains from the deep high-pressured mudstone into the reservoir (Flemings et al., 2002). As a result, the mudstone consolidates, and permeability becomes lower. Near the reservoir crest, the fluid escapes from the reservoir into the mudstone. Because of the high pressure fluid flow from the

deeper depth, the mudstone at the crest cannot be consolidated efficiently. I interpret that this characteristic mudstone permeability variation causes the reservoir to become more isolated from the deeper overpressure zone and more connected to the shallower overpressure zone.

The depth where reservoir pressure equals farfield mudstone pressure is controlled by the mudstone permeability contrast k_r. When we consider the effects of mudstone farfield vertical effective stress, reservoir structural relief, and mudstone compressibility, the key step is to analyze the permeability change of the mudstone that surrounds the reservoir. High reservoir structural relief and high mudstone compressibility lead to high permeability contrast; these conditions result in a shallower depth where reservoir pressure equals mudstone pressure. On the contrary, high stress conditions will lead to low permeability contrast, consequently, the depth where reservoir pressure equals mudstone pressure is deeper.

In our current static model, I assume a 2D rectangle shape for the reservoir geometry. A different geometry will lead to a different depth where reservoir pressure equals mudstone pressure. For example, a fan-shaped reservoir will tend to have more area exposed to the high overpressure zone because of its characteristic depositional geometry (Prather et al. 1998). In cases with complex geometry, the flow balance equation need to account for the geometry effect in calculating the permeability variation (k), and then obtain the depth where reservoir pressure equals mudstone pressure.

1.5 CONCLUSIONS

I use a static model to study the effect of permeability variation on overpressure and the relationship of sandstone and mudstone overpressure. The depth where reservoir pressure equals mudstone pressure is controlled by the permeability contrast of the

mudstone that surrounds the reservoir. A high mudstone permeability contrast leads to a shallower depth where reservoir pressure equals mudstone pressure and a low permeability contrast leads to a deeper equal pressure depth. High reservoir structural relief, low farfield mudstone vertical effective stress, and high mudstone compressibility are all likely to generate a high mudstone permeability contrast around the reservoir. A nomogram is constructed to determine the depth where reservoir pressure equals mudstone pressure based on the farfield mudstone vertical effective stress and structural relief. The nomogram illustrates that the higher the relief, the shallower the depth where reservoir pressure equals mudstone pressure, whereas the higher the farfield mudstone vertical effective stress, the lower the equal pressure depth.

I also construct basin models to characterize the permeability variation around the dipping reservoir and its effect on reservoir overpressure. I find that when mudstone permeability is constant, the reservoir overpressure equals to the farfield overpressure at the mid-point of the structure. When mudstone permeability is a function of vertical effective stress, the depth where reservoir pressure equals mudstone pressure is shallower than the mid-point of the structure.

I compare the pressure predicted by the static model with pressure obtained from two sources: basin model results and field pressure observations in Bullwinkle Basin. The pressures predicted by the static model agree better with the field pressure observations in Bullwinkle Basin than with the previous steady flow model results.

This study can be used to analyze the overpressure in dipping reservoirs in basins that have been mechanically compacted through burial. By offering a better understanding of the permeability effect on reservoir overpressure, it can help to analyze the trap integrity, understand hydrocarbon migration and reduce drilling incidences.

Table 1.3: Summary of models and key parameters

Run Number	e_0	σ_0'	C_c	A_k	B_k	R	σ'_{ms}(farfield)	Z
#	-	Mpa	-	$\log(m^2)$	$\log(m^2)$	m	Mpa	-
Run 1 (Static)	0.88	1	0.49	10.65	-23.1	500	5	0.31
Run 2 (Static)	0.88	1	0.49	10.65	-23.1	500	20	0.42
Run 3 (Static)	0.88	1	0.49	10.65	-23.1	1500	5	0.15
Run 4 (Static)	0.88	1	0.20	10.65	-23.1	500	5	0.43
Run 5 (Basin model)	0.88	1	0.49	0	-19	1100	-	0.50
Run 6 (Basin model)	0.88	1	0.49	10.65	-23.1	1100	10.5	0.27
Run 7 (Static)	0.88	1	0.49	10.65	-23.1	1100	10.5	0.26
Run 8 (Static)	0.88	1	0.49	10.65	-23.1	760	13	0.34

e_0, σ_0', C_c, A_k and B_k are mudstone property parameters, R is reservoir structural relief, σ'_{ms}(farfield) is farfield mudstone effective stress and Z parameter represents the position where reservoir pressure equals mudstone pressure.

Chapter 2: Data Report: Resedimentation and Consolidation Tests of Vilanova Tulo White Kaolin (VWK)

ABSTRACT

I conducted two resedimentation tests and two consolidation tests to study the physical properties and the compression behavior of the Vilinova Tulo White Kaolinite (VWK). The VWK Kaolinite is a low plasticity soil. Its liquid limit is 49%, plastic limit is 34%, and plasticity index is 15%. About 50% of the particles are smaller than 2μm. I prepared the specimens with a mass salinity of 3.4% (sea salt). During resedimentation, the porosity decreased from 70% to 58% as effective stress increase from 1.3kPa to 99kPa. The average estimated permeability of the two specimens is $4.90 \times 10^{-16} m^2$ under the stress of 99kPa. Constant-rate-of-strain (CRS) consolidation tests indicate that as the stress increased from 0.2MPa to 17.3Mpa, the porosity decreased from 58% to 30.0% and permeability decreased from about $2.94 \times 10^{-16} m^2$ to $4.21 \times 10^{-18} m^2$.

2.1 INTRODUCTION

The compression and permeability behavior of low-permeability sediments control pore pressure development and evolution, thus, they affect fluid flow. Understanding how sediments compress and expel their pore fluids during burial is important for pore pressure predictions and basin models. A series of geomechanical properties of VWK Kaolinite are studied in this research. The experimental results such as "void ratio vs. effective stress" and "porosity vs. permeability" are key input relationships in basin models.

The tested Kaolin is mined in Vilinova Tulo, Italy and processed by Mediterranean Basin Clays®. According to the supplier, VWK Kaolin contains 48~50% SiO_2, 35~37% Al_2O_3 and 0.6~0.8% Fe_2O_3. The CAS number of the material is 1332-58-7 (CAS registry number is assigned by the "Chemical Abstracts Service". It is a unique

numeric identifier to identify the chemical substance information). The grain density is $2.6 \times 10^3 kg/m^3$ (Details of "1332-58-7", 2012).

I first conducted Atterberg Limits tests to obtain the liquid limit (LL), plastic limit (PL) and the plastic index (PI) of the VWK Kaolinite. Then I performed resedimentation tests to simulate the deposition and burial of sediments in nature. At the end of the resedimentation test, the specimen was extruded and trimmed into a rigid ring for further consolidation testing. The geomechanical properties were measured and calculated through both resedimentation and CRS tests.

2.2 LABORATORY TESTING METHODOLOGY

2.2.1 Atterberg Limits tests

I used Atterberg limits tests to measure the liquid limit (LL), plastic limit (PL) and plastic index (PI) of the VWK Kaolinite. The detailed procedures and calculations are in **Appendix C**.

2.2.2 Grain size distribution

I performed three grain size analyses on VWK Kaolinite using hydrometer method in accordance to **ASTM D422-63(ASTM, 2007)**. Three grain size distribution tests on the VWK Kaolinite were performed to obtain consistent results.

2.2.3 Initial water content and salinity

I performed our resedimentation at a water content of 130%. This was the maximum water content at which the slurry was stable. Analysis of test tube experiments, where slurries prepared at different water contents are left in test tubes overnight, showed that a water content higher than 130% results in water separating from the slurry while a

water content lower than 130% results in the inability to pour the material easily. (**Appendix D**)

I want to resediment the material with a salinity that replicates the depositional environment. Thus, I performed our resedimentation test with a mass salinity of 3.4% (sea salt). To correctly determine how much salt needs to be added into the soil, I must first determine the mass of salt per unit dry mass of Kaolinite. I blended the Kaolinite to a certain amount of water and then used the salinity tester (conductor) to measure the salinity in the solution. From the measurements, I can calculate the amount of salt in the Kaolinite. VWK Kaolinite has 14.4mg salt per 100g dry soil. To make a slurry having a mass salinity of 3.4% and water content of 130%, I added 13.68g sea salt to 390g water, and mixed the salt water with 300g dry VWK Kaolinite thoroughly. The detailed procedure and calculations process are described in **Appendix E**.

2.2.4 Resedimentation

Resedimentation is a process to prepare homogeneous samples while simulating the natural deposition and burial of sediments. A key objective of resedimentation is to take out the large initial drop in porosity and prepare the specimens for later consolidation tests to much higher stresses.

After mixing all components thoroughly as described above and forming homogeneous slurry without any clumps, I used a vacuum pump to remove air bubbles in the slurry. After the vacuum, the slurry was poured into the consolidometer with a diameter of 69.2mm. Before adding any stress on the slurry in the consolidometer, the initial height is 12cm, and the initial void ratio e is 3.45. There are ten loading stages and a final unloading stage to an overconsolidation ratio of 4 in the resedimentation stage. The vertical displacements were recorded from the 4th loading increment and beyond.

The maximum load applied to the soil is 37.99kg, which is equivalent to 99.98kPa axial stress on the specimen. The details of the resedimentation procedure are described in **Appendix F** (Resedimentation Procedure).

2.2.5 Constant-rate-of-strain (CRS) consolidation test

Constant-rate-of-strain (CRS) consolidation tests (ASTM, 2006) consist of three major stages: loading stage, creep stage and unloading stage with a possible reload cycle at the end. During the loading stage, the specimen was compressed at a constant strain rate of 2% per hour. The maximum vertical effective stress is 17.6 MPa. After holding stress for 7 hours during the creep stage, the specimen was unloaded with a constant strain rate of 1% per hour to an overconsolidation ratio (OCR) of 4. At the end of the test, the specimen had a dimension of 4.98cm in diameter and 2.49cm in height. Compared with incremental loading (similar to the resedimentation test), the CRS test provides a continuous data set: a displacement transducer records the displacement of the specimen during the compression. In addition, because both the pore water pressure and the cell pressure are recorded through the test, the flow properties (hydraulic conductivity and permeability) can be measured directly as well.

2.3 LABORATORY TESTING RESULTS

2.3.1 Atterberg Limits and grain size distribution

The VWK Kaolin has a liquid limit (LL) of 49%, a plastic limit (PL) of 34% and a plastic index (PI) of 15%. **Fig. 2.1** shows a comparison of Atterberg Limits between the VWK Kaolin and other materials.

The grain size distribution tests show consistent results (**Fig. 2.2**). The grain size distribution is very narrow; this means that VWK Kaolinite has a small range of grain

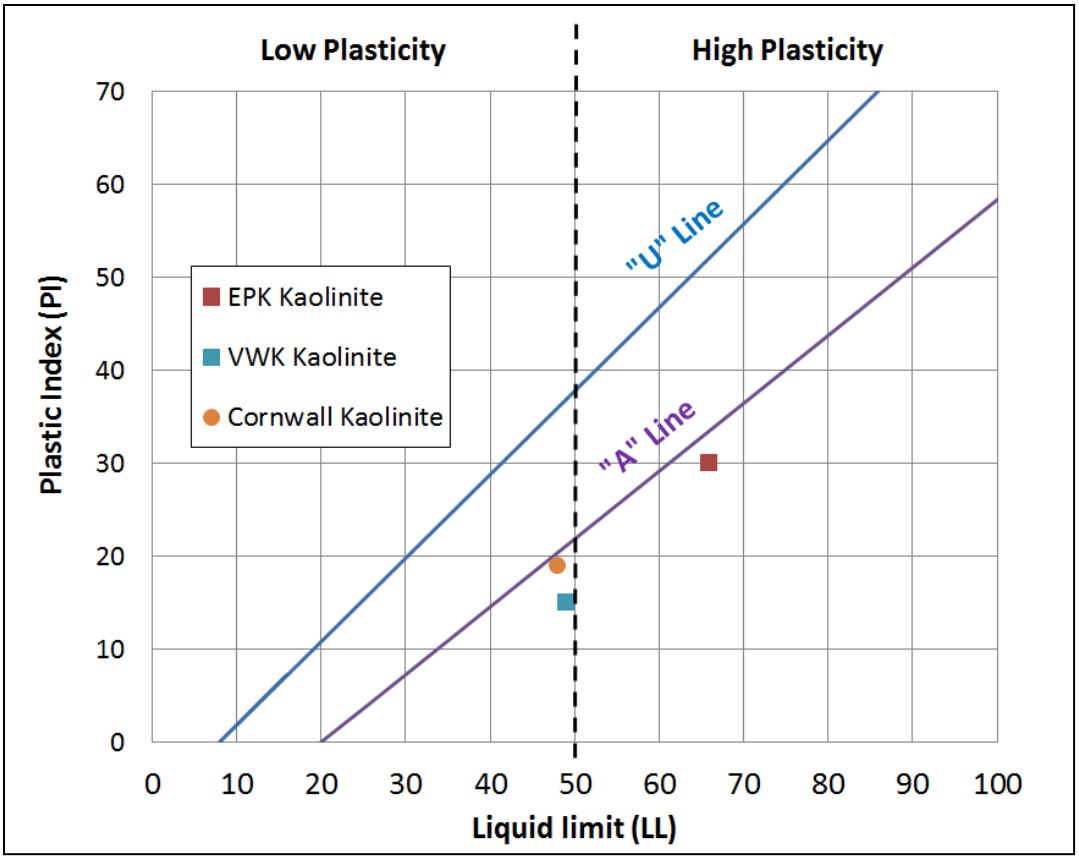

Figure 2.1: Plasticity chart

Above the A line, materials are defined as inorganic clay and below the line, they are defined as silt and organic clay. The material has a low plasticity if the Liquid limit (LL) is equal or smaller than 50% and has a high plasticity if the LL is higher than 50%. Because the LL of VWK Kaolinite is 49%, it has a low plasticity. The material plots below A-line. It indicates that it can be very delicate to handle.

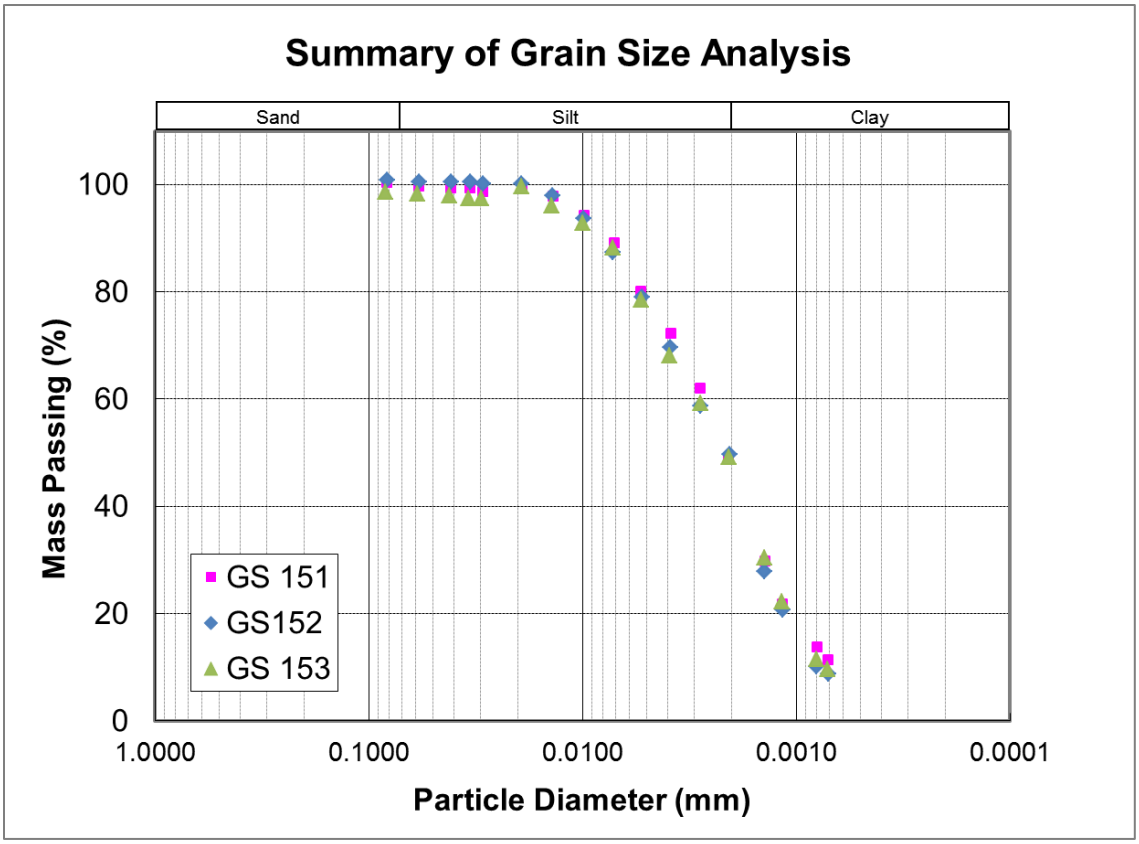

Figure 2.2: Summary of grain size distribution

sizes. **Fig. 2.2** shows that about 50% of the particles are smaller than 2 μm, which is defined as the boundary between silt-sized and clay-sized particles. In more detail, about 50% of the particles lie in the range of 20-2 μm (silt-size range) and about 40% of the clay-sized particles (< 2 μm) lie in the range of 2~0.7 μm. The remaining 10% of the clay-sized particles are smaller than 7 μm. The ratio of a soil is defined as the ratio of plastic index (PL) over the percentage of clay particles (less than 2μm). In this case, the activity is about 0.30 which is on the very low side of Kaolinite. This may reflect the fact that the material is processed.

2.3.2 Resedimentation

I performed two resedimentation tests. The test numbers are Resed68 and Resed69.

2.3.2.1 Load increment curves

The deformation of the specimens through time under constant loading was recorded by the displacement transducer. I measured the final height of the specimens with a manual scale at the end of the resedimentation tests. Then the height of the specimens at each incremental stage can be calculated.

The coefficient of consolidation is the parameter to describe the efficiency of the dissipation of the overpressure. It can be calculated from the relationship of the displacement and the square root of time relationship (Taylor's square root of time fitting method). (**Fig. 2.3**)

The graphical method to estimate the coefficient of consolidation (C_v) is summarized as follows:

1. Plot displacement vs. square root of time (black line)
2. Take the linear portion of the plot

3. Plot 1.15x vs. the displacement (the red line) and make a linear regression line
4. Take the intersection data point of the regression line and the black line (original data), the x axis value is the root time it takes to have 90% primary consolidation of the specimen.
5. Calculate C_v with the following equation:

$$C_v = \frac{0.848 \times d^2}{t_{90}} \qquad (1)$$

where d is the average drainage distance during increment and the t90 is the time from the construction method.

This gives the C_v values and the incremental deformation for each increment.

The relationship between coefficient of consolidation (C_v), permeability (k) and compressibility mv can be described in equation (2):

$$C_v = \frac{k}{m_v \cdot \mu} \qquad (2)$$

Table 2.1 and **Table 2.2** show the key results from the resedimentation tests. The corresponding calculations and discussions are in the following sections.

As the effective stress increases, the void ratio (e), porosity (n), compression index (C_c) and compressibility (m_v) decrease; the coefficient of consolidation (C_v) increases. The effective stress went up to 98.98kpa. Taking the average value over the two tests, the void ratio ranges from 2.85 to 1.36, the porosity ranges from 0.74 to 0.60, the compression index ranges from 1.1 to 0.15, the compressibility ranges from $6.5 \times 10^{-2} kPa^{-1}$ to $1.3 \times 10^{-4} kPa^{-1}$, coefficient of consolidation (C_v) ranges from $1.1 \times 10^{-8} m^2/s$ to $4.9 \times 10^{-7} m^2/s$ (**Fig. 2.4**), permeability ranges from $2.7 \times 10^{-15} m^2$ to $4.9 \times 10^{-16} m^2$.

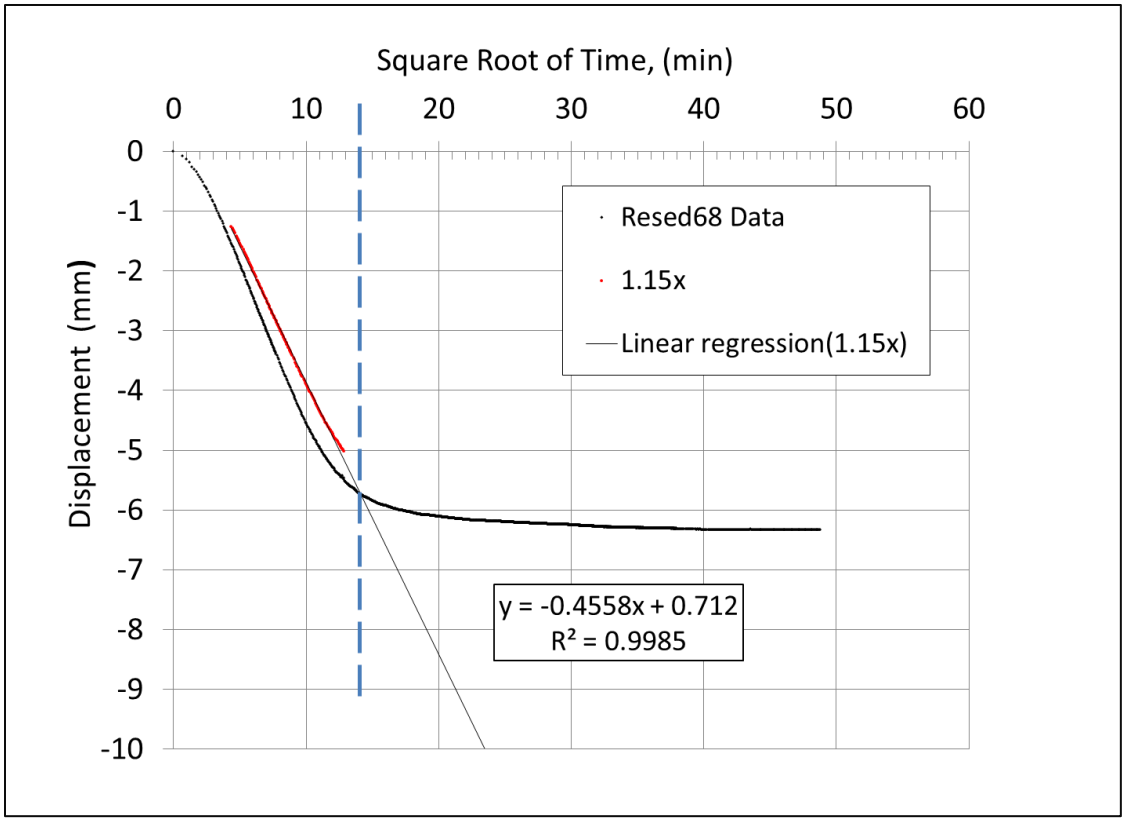

Figure 2.3: Displacement vs. Square root of time

Compression stage: resed68 at incremental 5 (effective stress = 5.2kPa). The black line shows the displacement change during compression. The red line shows the linear portion of the black line and then multiplies the square root time by 1.15.

Table 2.1: The key resedimentation test results (Reset068)

Inc	M	σ'	H_n	e_n	n	Cc	m_v	C_v	k
#	g	kPa	mm	-	-	-	kPa^{-1}	m^2/s	m^2
4 begin	490	1.28	84.46	2.68	0.73				
4	990	2.58	79.73	2.48	0.71	0.66	4.23E-02		
5	1990	5.18	72.11	2.15	0.68	1.08	3.61E-02	8.48E-08	3.06E-15
6	3990	10.40	66.33	1.90	0.66	0.82	1.51E-02	1.63E-07	2.45E-15
7	7990	20.82	61.88	1.71	0.63	0.63	6.30E-03	2.58E-07	1.63E-15
8	15990	41.66	58.01	1.55	0.61	0.55	2.93E-03	3.65E-07	1.07E-15
9	25990	67.72	55.32	1.43	0.59	0.55	1.74E-03	4.92E-07	8.56E-16
10	37990	98.98	53.54	1.36	0.58	0.46	1.00E-03	5.17E-07	5.18E-16
UN	9490	24.73	54.10	1.47	0.60	0.19	6.57E-04		

Inc: increment number; M: applied mass for each increment; σ': vertical effective stress; H_n: the height of the specimen; n: porosity; Cc: compression index; m_v: compressibility, C_v: coefficient of consolidation; k: permeability.

Table 2.2: The major resedimentation test results (Resed069)

Inc	M	σ'	H_n	e_n	n	Cc	m_v	C_v	k
#	g	kPa	mm	-	-	-	kPa^{-1}	m^2/s	m^2
4 begin	490	1.28	85.84	3.01	0.75				
4	990	2.58	76.13	2.56	0.72	1.47	8.63E-02	1.13E-08	9.79E-16
5	1990	5.18	70.18	2.28	0.70	0.91	2.98E-02	7.87E-08	2.34E-15
6	3990	10.40	62.28	1.91	0.66	1.21	2.14E-02	1.49E-07	3.19E-15
7	7990	20.82	57.90	1.71	0.63	0.67	6.70E-03	2.27E-07	1.52E-15
8	15990	41.66	54.31	1.54	0.61	0.55	2.94E-03	3.2E-07	9.40E-15
9	25990	67.72	51.93	1.43	0.59	0.52	1.67E-03	4.33E-07	7.22E-16
10	37990	98.98	50.26	1.36	0.58	0.47	1.02E-03	4.56E-07	4.65E-16
UN	9490	24.73	50.71	1.41	0.59	0.09	3.13E-04		

Inc: increment number; M: applied mass for each increment; σ': vertical effective stress; H_n: the height of the specimen; e_n: void ratio, n: porosity; Cc: compression index; m_v: compressibility, C_v: coefficient of consolidation; k: permeability.

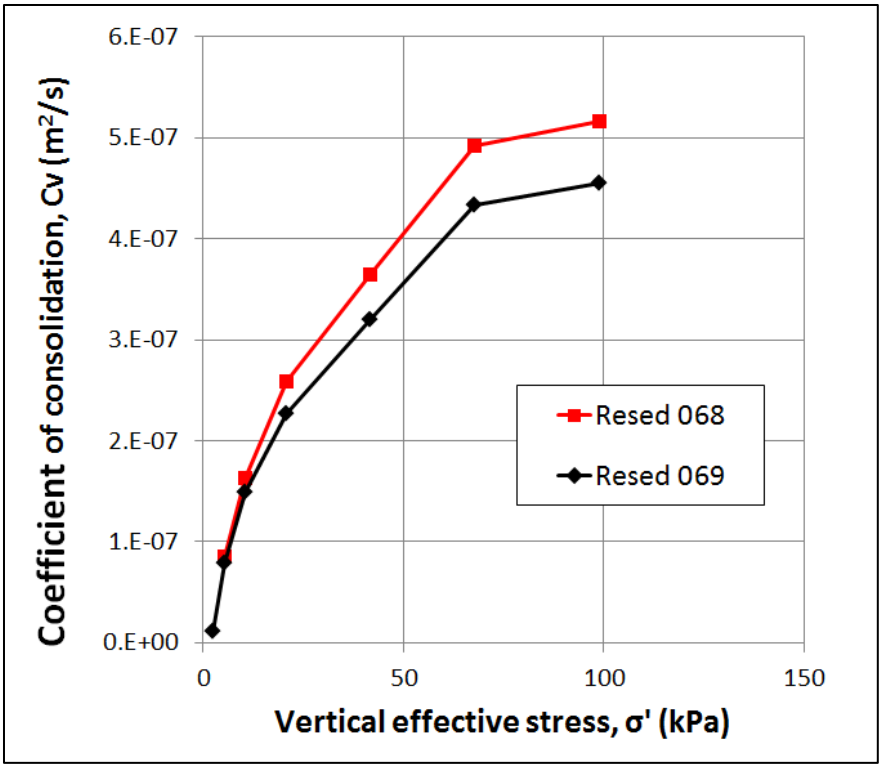

Figure 2.4: Coefficient of consolidation vs. vertical effective stress

2.3.2.2 Determination of void ratio at the end of resedimentation

The void ratio at the end of resedimentation is the initial void ratio computed for the CRS test specimen:

$$e_f = w_c \cdot G_s \quad (3)$$

Where, G_s is grain density (2.6kg/m3), wc is initial water content of the CRS test specimen (At the end of resedimentation tests, specimen Resed68 was trimmed to perform CRS100 test and specimen Resed69 was trimmed to perform CRS101 test). The initial water content for CRS 100 and CRS101 are 56.7% and 54.3% respectfully. Because the grain density of VWK Kaolinite is 2.6g/cm^3, then the void ratios at the end of the resedimentation tests are 1.47 (Resed 68) and 1.41(Resed 69).

2.3.2.3 Determine void ratio at each loading stage

Once the void ratio at the end of the resedimentation test is determined, void ratios at other stages can be calculated from displacement measurements: (**Table 2.3, Table 2.4**)

$$e_n = \frac{H_f\left(\frac{e_f}{1+e_f}\right)+H_n-H_f}{\frac{H_f}{1+e_f}} \quad (4)$$

where e_n is void ratio at the stage n (n=1,2,…,9,10), e_f is final void ratio (stage #10), H_f is final height of the specimen (stage #10), and H_n is the height of the specimen at increment n.

2.3.2.4 Compression Curves

Fig. 2.5 illustrates the compression behavior during the loading and unloading stages during resedimentation. As the effective stress increased up to about 100 kPa, void ratio decreased from about 2.8 to 1.4 approximately.

Table 2.3: Specimen height and void ratio at each stage (Resed 068)

Inc	M	σ'	L	Δh	H_n	e_n
#	g	kPa	mm	mm	mm	-
4 begin	490	1.28	0.00	0.00	84.46	2.68
4	990	2.58	4.73	4.73	79.73	2.48
5	1990	5.18	12.35	7.62	72.11	2.15
6	3990	10.40	18.13	5.77	66.33	1.90
7	7990	20.82	22.58	4.45	61.88	1.71
8	15990	41.66	26.45	3.87	58.01	1.55
9	25990	67.72	29.14	2.69	55.32	1.43
10	37990	98.98	30.92	1.78	53.54	1.36
UN	9490	24.73	30.36	-0.56	54.10	1.47

Inc: increment number; M: applied mass for each increment; σ': vertical effective stress; L: total displacement; Δh: displacement during each stage, H_n: specimen height at each stage, e_n: void ratio at stage n

Table 2.4: Specimen height and void ratio at each stage (Resed 069)

Inc	M	σ'	L	Δh	H_n	e_n
#	G	kPa	mm	mm	mm	-
4 begin	490	1.28	0.00	0.00	85.84	3.01
4	990	2.58	9.71	9.71	76.13	2.56
5	1990	5.18	15.66	5.95	70.18	2.28
6	3990	10.40	23.55	7.89	62.28	1.91
7	7990	20.82	27.94	4.39	57.90	1.71
8	15990	41.66	31.52	3.58	54.31	1.54
9	25990	67.72	33.90	2.38	51.93	1.43
10	37990	98.98	35.58	1.67	50.26	1.36
UN	9490	24.73	35.13	-0.45	50.71	1.41

Inc: increment number; M: applied mass for each increment; σ': vertical effective stress; L: total displacement; Δh: displacement during each stage, H_n: specimen height at each stage, e_n: void ratio sta stage n

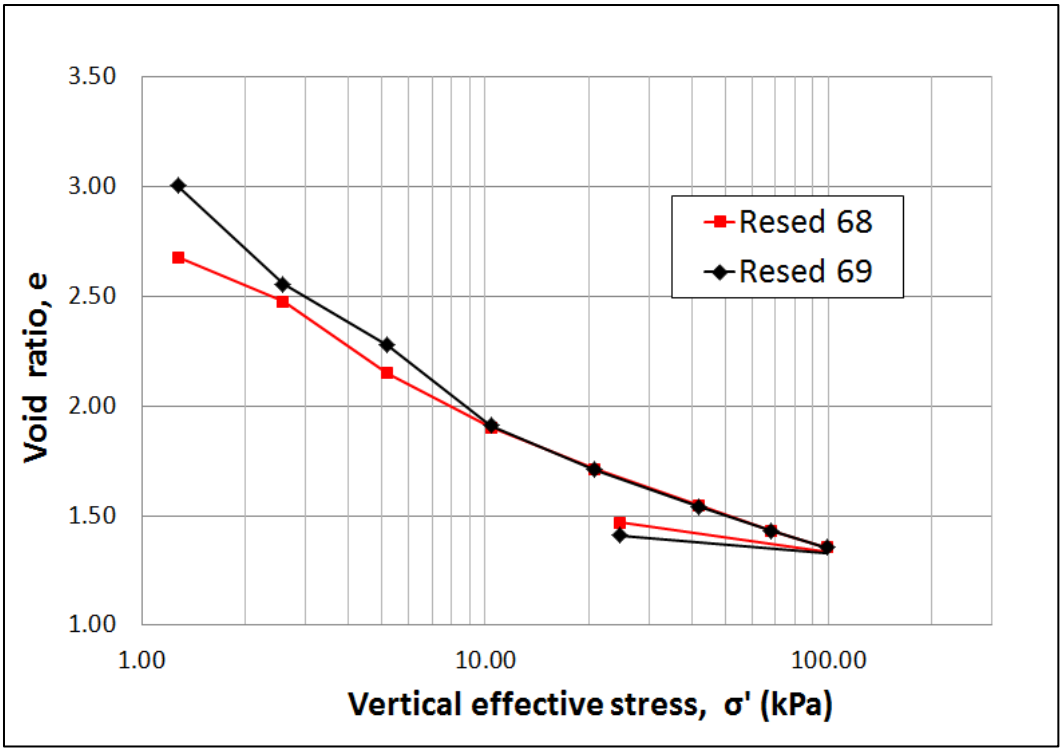

Figure 2.5: Void ratio vs. vertical effective stress

2.3.2.5 The compression index

The compression index (C_c, **Table 2.5**) describes the slope of the compression curve. C_c can also reflect the stiffness of the material. It is defined as:

$$C_c = \frac{e_0 - e_1}{\log(\frac{\sigma_1'}{\sigma_0'})} \qquad (5)$$

Overall, as the axial applied stress increased, the compression index decreased from 1.47 to 0.47. This indicates the specimen becomes stiffer.

2.3.2.6 The compressibility

Compressibility (mv) describes the stiffness of the material. m_v can be calculated by using the following equation:

$$m_v = \frac{1}{1+e_0} \cdot \frac{e_0 - e_1}{\sigma_1' - \sigma_0'} \qquad (6)$$

Fig. 2.6 illustrates the compressibility of the VWK Kaolin at each loading stage. I can see that as the vertical stress increased, the compressibility of the specimens decreased. The compressibility decreased very fast at the beginning (for stresses lower than 20 kPa). Then it became harder to be compressed.

2.3.2.7 The permeability

The permeability can be evaluated from the following equation:

$$k = C_v \cdot m_v \cdot \mu \quad (7)$$

where k is permeability, C_v is the coefficient of consolidation, mv is compressibility and μ is dynamic viscosity at the test temperature. I assumed a viscosity of 0.001Ps/s. The evaluated values are listed in **Table 2.1** and **Table 2.2**. **Fig. 2.7** shows the relationship of porosity and permeability. The log of permeability varies linearly with porosity. Permeability decreased from $2.36 \times 10^{-15} m^2$ to $5.0 \times 10^{-15} m^2$ as porosity decreased from 0.68 to 0.56 (the steady-state part of the test).

Table 2.5: Compression index (C_c) during each stress interval

Stress Interval	C_c (Resed068)	C_c (Resed069)
1.3~2.6kPa	0.66	1.47
2.6~5.2kPa	1.08	0.91
5.2~10.4kPa	0.82	1.21
10.4-20.8kPa	0.63	0.67
20.8-41.7kPa	0.55	0.55
41.7-67.7kPa	0.55	0.52
67.7-99.0kPa	0.46	0.47

Table 2.6: Compression indices at various stress intervals

σ' (Mpa)	C_c (CRS100) (Mpa^{-1})	C_c(CRS101) (Mpa^{-1})
5~8	0.389	0.366
8~11	0.390	0.368
11~14	0.383	0.356
14~17	0.359	0.340

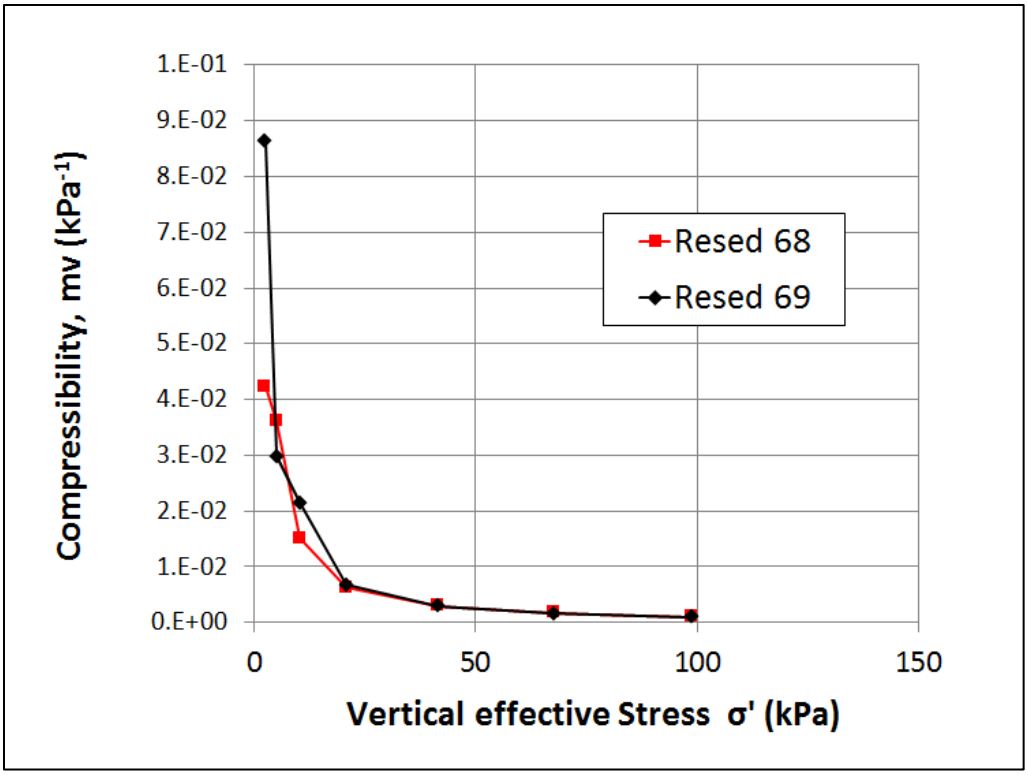

Figure 2.6: Compressibility vs. Vertical effective stress

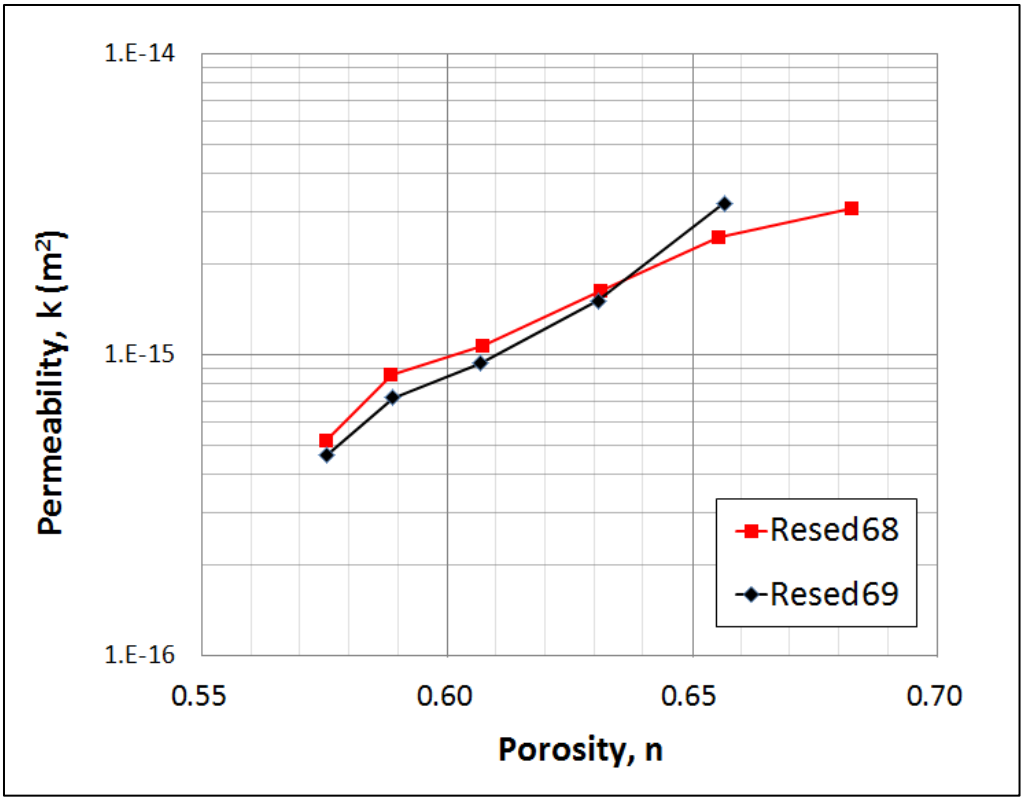

Figure 2.7: Permeability vs. porosity relationship from Resedimentation tests

2.3.3 Constant-rate-of strain (CRS) consolidation

2.3.3.1 Summary of CRS tests

I performed two CRS tests: CRS100 and CRS101. The specimen for CRS100 was trimmed from Resed68 and specimen CRS101 was trimmed from Resed69. **Appendix G** shows the plots of the results from both CRS tests.

Vertical effective stress (σ'), void ratio (e), compressibility (m_v), hydraulic conductivity (K) and coefficient of consolidation (C_v) were calculated from the following equations (ASTM, 2006):

$$e = \frac{H - H_s}{H_s} \quad (8)$$

$$\sigma' = \sigma_v - \frac{2}{3}\Delta u \quad (9)$$

$$K = \frac{\frac{d\varepsilon}{dt} \cdot H_0 \cdot H \cdot \gamma_w}{2\Delta u} \quad (10)$$

$$m_v = \frac{\Delta\varepsilon}{\sigma'} \quad (11)$$

$$C_v = \frac{K}{m_v \cdot \gamma_w} \quad (12)$$

Hydraulic conductivity then converted to permeability with:

$$k = K\frac{\mu}{\rho_l \cdot g} \quad (13)$$

2.3.3.2 Compression curves and Compression index from CRS tests

Fig. 2.8 and **Fig. 2.10** shows the compression curves of the two CRS tests results. The two curves are very similar. From these curves, I can see at lower stress (<100kpa), the material has a low gradient (relative flat) and the gradient becomes higher when the stress passes 100kpa.

100kPa is the preconsolidation stress, which separates elastic behavior from the plastic behavior in the tests. Below 100kPa, the deformation is mostly elastic behavior; above than 100kPa, the deformation is mostly plastic behavior. **Table 2.6** is the summary

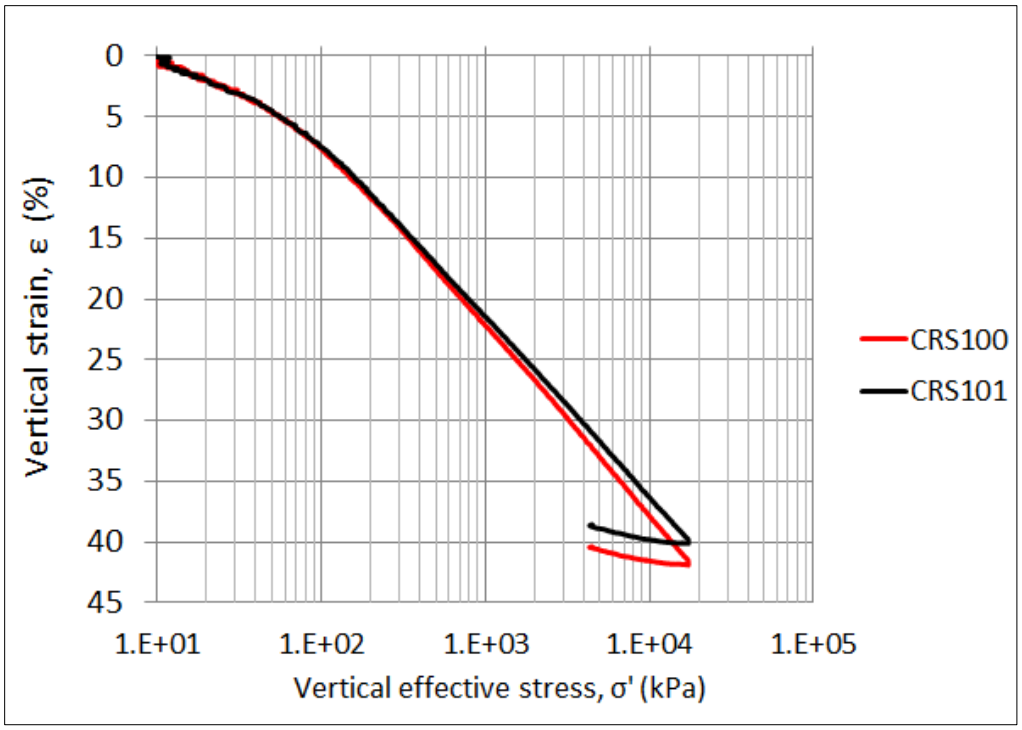

Figure 2.8: Vertical strain vs. Vertical effective stress for CRS100 and CRS101

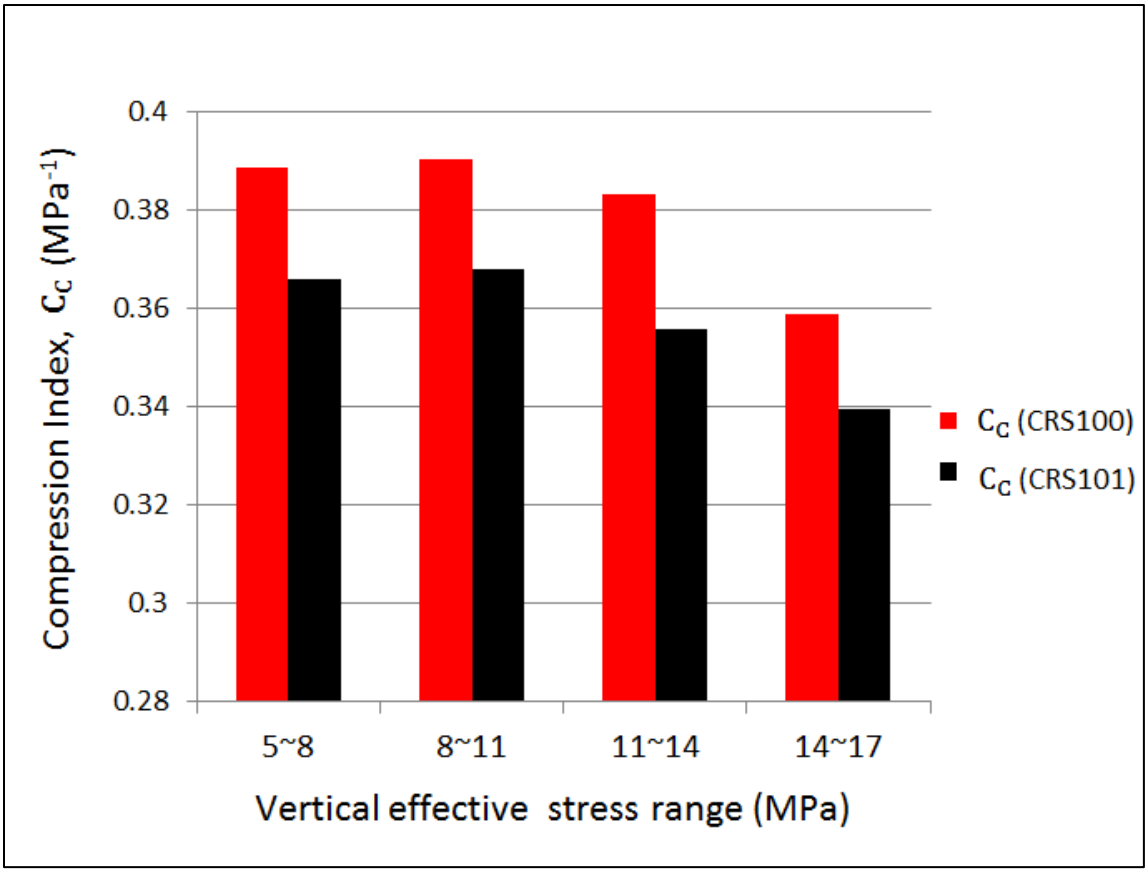

Figure 2.9: Compression index at various stress intervals;

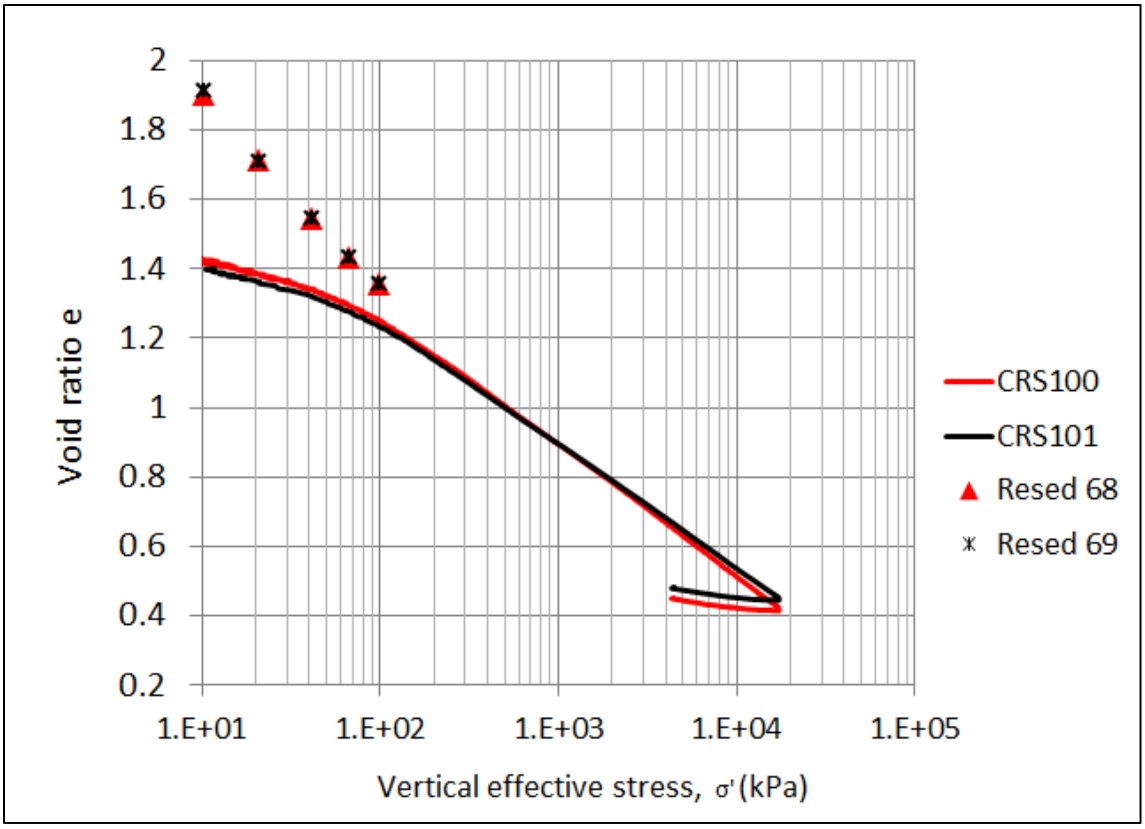

Figure 2.10: Void ratio vs. Vertical effective stress (Combining the resedimentation and CRS results)

of the compression indices at various stress intervals. Recall the equation for calculating the compression index:

$$C_c = \frac{e_0 - e_1}{\log(\frac{\sigma_1'}{\sigma_0'})} \qquad (5)$$

From the **Fig. 2.9**, I see that the C_c value is a little lower at the axial stress interval of 8~11 MPa than that at the effective stress interval of 8~11MPa. Above 8MPa (to 17MPa), the C_c value continues to decrease gradually.

2.3.3.3 Permeability from CRS tests

Fig. 2.11 shows the porosity and permeability relationship from the CRS tests. As the porosity decreases from 0.58 to 0.30, the permeability decrease from $2.94\times10^{-16} m^2$ to $4.21\times10^{-18} m^2$. From the results, I can see that log(k) has a linear relationship with porosity. The results from both tests are consistent. I made linear regression between log(k) and porosity for both tests:

CRS100: log(k) = 6.61n-19.33 (14)

CRS101: log(k)= 6.74n-19.48 (15)

By combing the results from the resedimentation experiments (**Fig. 2.12**), I can see that the porosity and permeability relationship over a larger range.

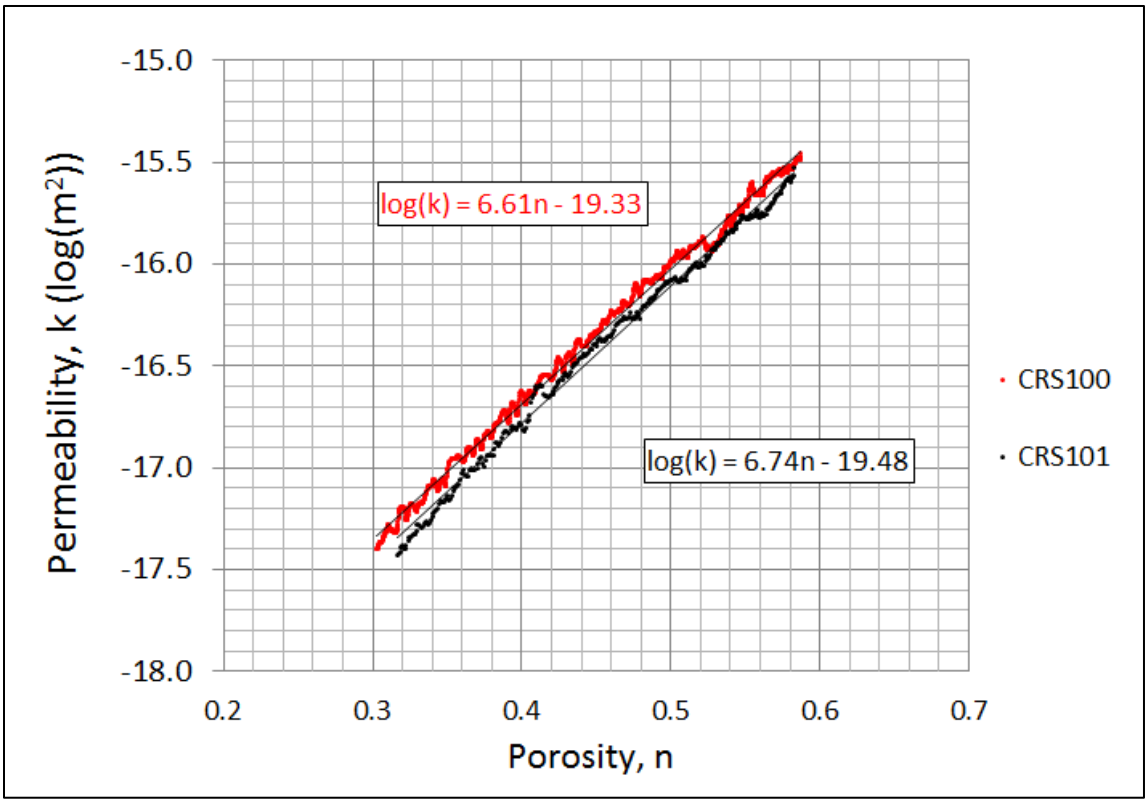

Figure 2.11: Permeability vs. porosity from CRS test results

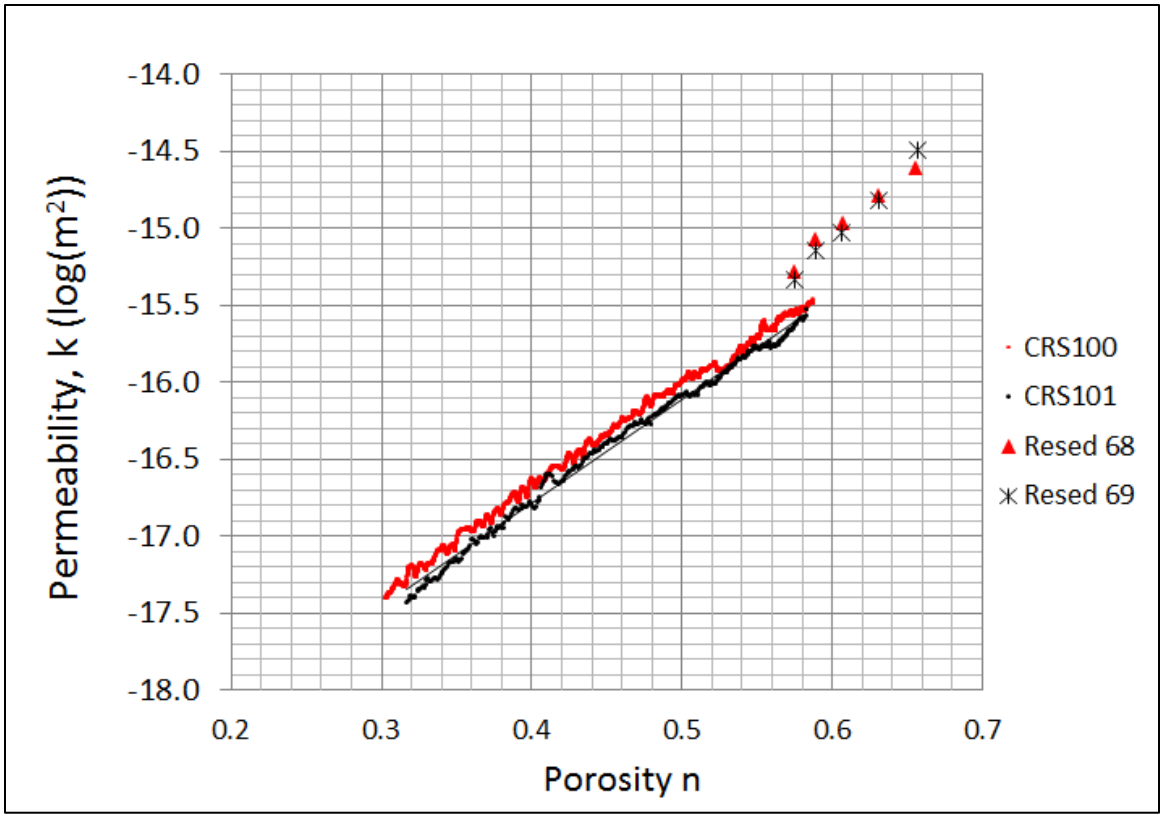

Figure 2.12: Permeability vs. porosity from CRS test results and resedimentation experiments

Table 2.7: Nomenclature (Chapter2)

Variable	Definition	Dimension	Unit
C_c	Compression index	Dimensionless	-
C_v	Coefficient of consolidation	L^2/T	m^2/s
d	Average drainage distance	L	mm
e	Void ratio	Dimensionless	-
e_f	Void ratio at final stage	Dimensionless	-
e_n	Void ratio at stage n	Dimensionless	-
G_s	Grain density	M/L^3	g/cm^3
H	Height of specimen	L	mm
H_n	Specimen height at stage n	L	mm
H_f	Specimen height at final stage	L	mm
H_s	Equivalent height of solid	L	mm
Δh	Displacement between each load	L	mm
L	Total displacement	L	mm
m_v	Compressibility	LT^2/M	1/kPa
M	Mass of added load	M	g
K	Hydraulic conductivity	L/T	m/s
n	Porosity	Dimensionless	-
OCR	Over consolidation ratio	Dimensionless	-
w	Water content	Dimensionless	-
w_c	Initial water content	Dimensionless	-
σ'	Vertical effective stress	M/LT^2	kPa
σ_v	Applied vertical stress	M/LT^2	kPa
μ	Viscosity	$ML^{-1}T^{-1}$	Pa.s
ε	Strain	Dimensionless	-
ρ	Density	$ML\_^3$	kg/m^3
γ_w	Unit weight of water	$ML^{-2}T^{-2}$	kN/m^3

Appendix A: Static Model

I combine Darcy's Law with volume conservation and assume that the flux into the reservoir equals the flux out of the reservoir:

$$\int_{z_1}^{z_2} Q(z)dz = \int_{z_1}^{z_2} \frac{-k_i(z)}{\mu} \cdot dA \cdot \left(\frac{u^*_{res} - u^*_{ms}}{dx}\right) = 0 \quad (1)$$

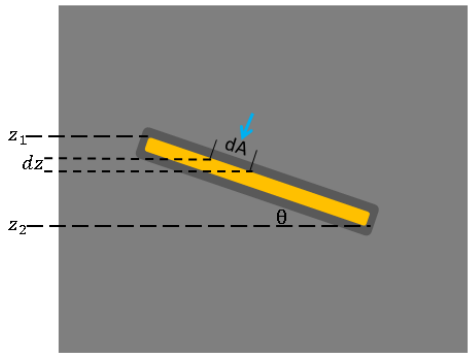

Figure A.1: Sketch of static model.

z_1 and z_2 are the crest and base of the dipping reservoir respectfully. The dipping angle of the reservoir is θ.

The area (dA) is:

$$dA = \frac{(dz)}{cos\theta} \cdot dy \quad (2)$$

I combine equation 1 and 2

$$\int_{z_1}^{z_2} \frac{-k_i(z)}{\mu} \cdot \left(\frac{dz}{cos\theta} \cdot dy\right) \cdot \left(\frac{u^*_{res} - u^*_{ms}}{dx}\right) = 0 \quad (3)$$

If μ, $cos\theta$ (assume the surface of the dipping reservoir is a flat plane), dx and dy are constant, then I obtain the following format:

$$\int_{z_1}^{z_2} -k_i(z) \cdot dz \cdot (u^*_{res} - u^*_{ms}) = 0 \quad (4)$$

Equation 4 can be discretized as follows:

$\sum_{i=1}^{n} k_i(z) \cdot dz \cdot \left[u^*_{ms(i)}(z) - u^*_{res}\right] = 0$ (5)

To solve Eq. 5, we need to know the relationship between vertical effective stress and permeability and we need to know the vertical effective stress in the mudstone at any depth. Our approach is as follows.

I assume the overpressure in the sandstone must lie somewhere between the mudstone overpressure at the top of the reservoir and the mudstone overpressure at the base of the reservoir;

I assume overburden stress σ_v and hydrostatic pressure u_h increase linearly with depth.

$\sigma_v = m_1 z + b_1$ (6)

$u_h = m_2 z + b_2$ (7)

Then the reduced lithostatic pressure u^*_{litho} is

$u^*_{litho} = \sigma_v - u_h = m_3 z + b_3$ (8)

Where $m_3 = m_1 - m_2,\ b_3 = b_1 - b_2$

The farfield mudstone overpressure u^*_{ms} is assumed to have a linear relationship with depth and the overpressure gradient is assumed to equal the reduced lithostatic pressure gradient:

$u^*_{ms} = m_3 z + b_4$ (9)

In an ideal connected dipping reservoir, the reservoir overpressure is identical. In the first trial, I assume the depth where reservoir overpressure equals farfield mudstone overpressure at the crest of the reservoir z_1,

$u^*_{res} = u^*_{ms}(z_1) = m_3 z_1 + b_4$ (10)

Surrounding the reservoir, the mudstone overpressure is close to the reservoir overpressure:

u^*_{ms} (surrounding) $\approx u^*_{res} = m_3 z_1 + b_4$ (11)

Under this condition, the mudstone vertical effective stress surrounding the reservoir can be calculated as follows:

$\sigma'_{v(ms)}\,(surrounding) = u^*_{litho} - u^*_{res} = m_3 z + b_3 - (m_3 z_1 + b_4) = m_3 z - m_3 z_1 + b_5$ (12)

Where $b_5 = b_3 - b_4$

Therefore, the mudstone vertical effective stress increases linearly with depth surrounding a dipping reservoir.

With the vertical effective stress, I calculate permeability in the surrounding mudstone according to the compression model and permeability model. The lithology parameters I use here is from the CRS test results. The mudstone sample is from Eugene Island and has 65% clay fraction (Betts, 2013 thesis).

The compression model of the mudstone:

$e = 0.88 - 0.49 \log(\sigma'_v)$ (13)

where e is void ratio, σ'_v is vertical effective stress and void ratio e is a function of porosity ϕ:

$\phi = \frac{e}{1+e}$ (14)

The relationship between mudstone permeability and mudstone porosity is defined:

$$\log(k) = 10.65\phi - 23.1 \quad (15)$$

Combine Eq. 13, Eq.14 and Eq.15, I obtain the mudstone permeability is function of the mudstone vertical effective stress:

$$k = 10^{10.65 \cdot \frac{0.88 - 0.49\log(\sigma_v')}{1.88 - 0.49\log(\sigma_v')} - 23.1} \quad (16)$$

Substitute Eq. 12 to Eq. 16, the mudstone permeability surrounding the reservoir is:

$$k(surrounding) = 10^{10.65 \cdot \frac{0.88 - 0.49\log(m_3 z - m_3 z_1 + b_5)}{1.88 - 0.49\log(m_3 z - m_3 z_1 + b_5)} - 23.1} \quad (17)$$

Combine Eq. 9 and Eq. 10:

$$u_{ms}^* - u_{res}^* = m_3 z - m_3 z_1 \quad (18)$$

Calculate the total flux by substitute Eq17 and Eq.18 to the following equation:

$$Q = \int_{z_1}^{z_2} Q_i = \int_{z_1}^{z_2} \frac{-\mathrm{k_i}(z)}{\mu} \cdot \mathrm{dA} \cdot \left(\frac{\mathrm{u_{res}^* - u_{ms}^*}}{\mathrm{dx}}\right) \quad (19)$$

I find:

$$Q = \int_{z_1}^{z_2} - 10^{10.65 \times \frac{0.88 - 0.49\log(m_3 z - m_3 z_1 + b_5)}{1.88 - 0.49\log(m_3 z - m_3 z_1 + b_5)} - 23.1} \cdot \frac{dA}{\mu \cdot dx} \cdot (m_3 z - m_3 z_1) \qquad (20)$$

Similarly, I calculate the total flux by assuming reservoir overpressure equals mudstone overpressure at depth of (z_1+dz). For this case, the total flux is:

$$Q = \int_{z_1}^{z_2} - 10^{10.65 \times \frac{0.88 - 0.49\log(m_3 z - m_3 (z_1 + dz) + b_5)}{1.88 - 0.49\log(m_3 z + b_3 - [m_3 (z_1 + dz) + b_4])} - 23.1} \cdot \frac{dA}{\mu \cdot dx} \cdot (m_3 z - m_3 (z_1 + dz))$$

I iterate through potential depth where reservoir overpressure equals mudstone overpressure (z_1, z_1+dz, z_1+2dz…. z_2-dz, z_2) and calculate the total flux for each case. I then determine the true depth where reservoir overpressure equals farfield mudstone overpressure and true reservoir overpressure is the case that yields Q = 0 (satisfy volume conservation).

Appendix B: Constant Permeability Case

Simplified flow balance equation is:

$$\int_{z_1}^{z_2} -k_i(z) \cdot (u^*_{res} - u^*_{ms}) \cdot dz = 0 \quad (1)$$

Eq. 1 can be written in the following form:

$$\int_{z_1}^{z_2} k_i(z) \cdot u^*_{res} \cdot dz = \int_{z_1}^{z_2} k_i(z) \cdot u^*_{ms} \cdot dz \quad (2)$$

Now consider a simple case: permeability k is a constant value. Then the $k_i(z)$ term can be cancelled out:

$$\int_{z_1}^{z_2} u^*_{res} \cdot dz = \int_{z_1}^{z_2} u^*_{ms} \cdot dz \quad (3)$$

$$u^*_{res} = \frac{\int_{z_1}^{z_2} u^*_{ms} \cdot dz}{z_2 - z_1} \quad (4)$$

Assume u^*_{ms} is a linear function of depth:

$u^*_{ms} = cz + a$, (5)

Where c is the gradient of the farfield mudstone overpressure and a is the intercept.

Substitute Eq. 5 to Eq. 4 and solve for u^*_{res}:

$$u^*_{res} = \frac{\int_{z_1}^{z_2} u^*_{ms} \cdot dz}{z_2 - z_1} = \frac{\int_{z_1}^{z_2} (cz + a) \cdot dz}{z_2 - z_1} = \frac{\left(\frac{1}{2}cz_2^2 + az_2\right) - \left(\frac{1}{2}cz_1^2 + az_1\right)}{z_2 - z_1}$$

$$= \frac{\frac{1}{2}c(z_2^2 - z_1^2) - a(z_2 - z_1)}{z_2 - z_1} = \frac{\frac{1}{2}c(z_2 - z_1)(z_2 + z_1) - a(z_2 - z_1)}{z_2 - z_1}$$

$$= \frac{1}{2}c(z_2 + z_1) - a$$

$$u^*_{res} = c \cdot \underbrace{\frac{1}{2}(z_2 + z_1)}_{\textbf{Midpoint}} - a$$

Appendix C: Determination of Atterberg Limits

C.1 MEASURE LIQUID LIMIT (LL)

I use the Casagrande cup method to test the liquid limit.

For more details, please read ASTM-D4318-05(ASTM, 2005).

C.1.1 Summary of the LL test procedure

1. Weigh 150g Kaolinite and mix it thoroughly with DI water in a mixing bowl.
2. Using a spatula, place part of the prepared soil to the cup. Spread it in the cup to have a horizontal surface. The deepest point should have a depth of about 10mm.
3. Form a groove in the soil pat with the growing tool. The beveled edge was drawn forward through the soil from the highest point to the lowest point on the rim of the cup. Maintain the tool perpendicular to the surface of the cup through drawing.
4. Lift and drop the cup by turning the crank at the rate of 1.9 to 2.1 drops per second until the two halves of the soil come in contact at the bottom of the groove along a distance of 13mm. Use a scale to have quick checks during the process.
5. Record the numbers of the drops, N, required to close the groove. Remove a slice of the soil to put it into a dry tare with known mass. Take the moist mass and then put it into the oven.
6. Return the remaining soil in the cup to the mixing bowl. Remix the soil in the mixing bowl and clean the cup.
7. Repeat steps 2~6 to have one closure requiring 25 to 35 blows, one closure requiring 20 to 30 blows and one closure between 15 and 25 blows.
8. Determine the water content W^n for each trial

The liquid limit test data are shown in **Table C.1**

C1.2 Determine the liquid limit

1. Plot the relationship of water content w^n and the corresponding number of drops N of the cup on a semilogarithmic graph. Set water content as the ordinates on the arithmetical scale and the number of the drops as abscissas on a logarithmic scale.
2. Make a straight regression line through the three(or more) plotted points
3. Take the water content when N is 25 according to the regression line. (The water content is 0.4913 when N is 25) Then, the liquid limit is determined as 49. (**Fig. C.1**)

C.2 MEASURE PLASTIC LIMIT (PL)

C.2.1 Summary of the PL test procedure

1. Select 1.5 to 2.0g soil from the mixing bowl (the rest material used for LL test). Form the selected portion into an ellipsoidal mass.
2. Roll the mass between the palm or fingers on the glass plate to form a thread of uniform diameter throughout its length. When the diameter of the thread become 3.2mm, breakdown the thread into several pieces. Squeeze the pieces together and re-roll.
3. Repeat 2 until the soil can no longer form a 3.2-mm diameter thread.
4. Put the soil in a dry tare with known mass. Cover the tare with a plastic wrap to prevent evaporation.
5. Repeat 1~4 until there are at least 6 g soil in the tare
6. Dry it in the oven and calculate the average water content

C.2.2 Determine the plastic limit

Compute the average of the water contents and round to the nearest whole number. This is the value of the plastic limit, PL. For our test, PL is calculated as 34. (**Table C.2**)

C.3 DETERMINE THE PLASTICITY INDEX (PI)

PI = LL – PL = 49-34 =15

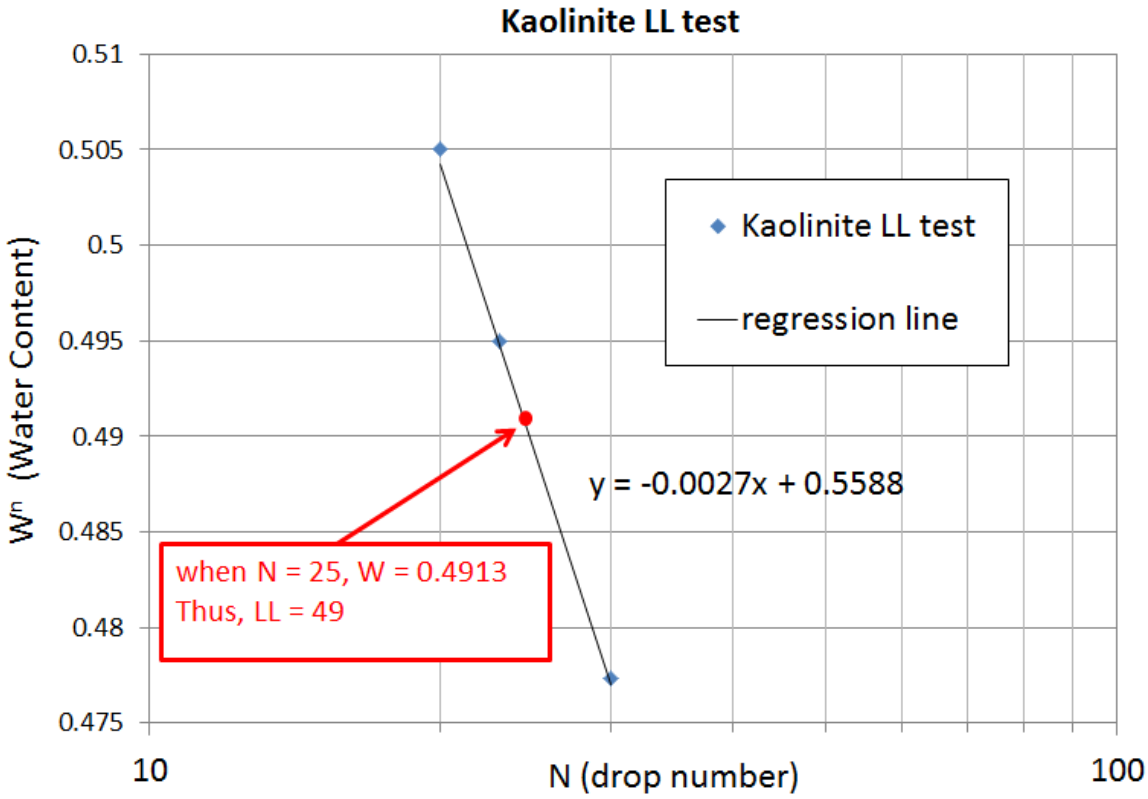

Figure C.1: Water Content vs. Drop Number

Table C.1: Liquid Limit test data

Trial number	1	2	3
Tare mass (g)	45.82	45.66	47.02
Tare mass+Wet mass (g)	57.8	60.58	62.99
Tare mass+Dry mass (g)	53.78	55.64	57.83
Drop Number, N	20	23	30
Water Content, W	0.505	0.495	0.477

Table C.2: Plastic Limit test data

Tare mass	21.09
Tare mass + Wet mass (g)	30.82
Tare mass + Dry mass (g)	28.33
Water content	0.344
PL	34

Appendix D: Determine the resedimentation water content

Settling analysis is done in the test tubes to determine the appropriate water content for resedimentation. If the water content is too low, it is hard to pour the slurry into the consolidometer. If the water content is too high, particle segregation results with the coarser particles settling to the bottom of the tube.

Note: the amount of salt in the slurry will affect the water content corresponding to stable slurry.

D.1 Summary of the tube test procedure

1. Take 20g Kaolinite and measure the mass of water according to the water contents that we want to test.
2. Mix the water and Kaolinite thoroughly in a small beaker.
3. Pour the mixture into a test tube with a funnel. (Avoid having too much soil stick on the glass. It will block your view to observe settlement)
4. Insert a rubber stopper on the top of the test tube to keep the soil saturated with water.
5. Observe the test tube over several days to see if segregation occurs.

The tube test data are shown in **Table D.1** and water content can be calculated by Eq. (D.1)

$$w = \frac{m_w}{m_s} \quad \textbf{(D.1)}$$

Where w is the water content, m_w is the mass of water and m_s is mass of the specimen.

D.2 Determine the appropriate water content

I find that at a water content of 120%, it's difficult to pour the material out. At a water content of 130%, no segregation occurs and the material can pour easily. At a water content of 140%, even though there is no segregation either, it will take a much longer

time to settle down because of its high water content. Thus, I determine to use 130% as the water content to run the resedimentation tests.

Table D.1: Tube test data

solid mass	water content	water mass
(g)	(%)	(g)
20	120	24.01
20.01	130	26.01
20	140	28.01

Appendix E: Measure the salt content and determine the mass of added salt

E.1 SALT CONTENT

I blend the Kaolinite to a certain amount of water and then use the salinity tester (conductor) to measure the salinity in the solution. According to the results, I can back calculate the amount of salt in the Kaolinite.

E.1.1 Summary of the salinity test procedure

1. Take 15g Kaolinite and 100g water.
2. Mix the water and Kaolinite in a small beaker. Agitating the mixture in an ultrasonic bath for about 20 minutes to dissolve the salt completely.
3. Transfer the mixture to a bottle and twist the cap firmly.
4. Place the bottle in a centrifuge for 30 minutes with the rotation speed of 10,000RPM
5. Open the bottle and transfer the solution to a small beaker
6. Measure the salinity of the solution

The salinity test results are shown in **Table E.1**

E.1.2 Determine the salt content

Average salinity: $\frac{22.1+21.1}{2}\left(\frac{\text{mg}}{\text{L}}\right) = 21.6\left(\frac{\text{mg}}{\text{L}}\right)$

Mass of salt in per 100g liquid: $\left(\frac{100\text{g}}{1000\text{g}}\right)\text{L} * 21.6\left(\frac{\text{mg}}{\text{L}}\right) = 2.16\text{mg}$

Thus, I know there is 2.16mg salt in per 15g VWK Kaolinite.

For per 100g VWK Kaolinite, the salt content can be calculated as:

$$\frac{2.16\text{g}}{15\text{g}} * 100\text{g} = 14.4\text{mg}$$

E.2 DETERMINE THE ADDED WATER MASS AND SALT MASS

My goal is to make a specimen saturated with salt water with a salinity of 3.4%.

Initial water content: 130%; Mass of Kaolinite: 300g.

E.2.1 Determine the mass of water

Mass of water: 300g*130% = 390g

E.2.2 Determine the mass of added sea salt

VWK salt needed: $\frac{\text{VWK mass of salt}}{\text{mass of salt + mass of water}} = 3.4\%$， VWK mass of salt = 13.72671g

Salt in Kaolinite = 300g* 14.4mg/100g = 43.2mg = 0.0432g

Salt added = VWK mass of salt – salt in Kaolinite = 13.72671g-0.0432g = 13.6835g

Table E.1: Salt content test data

test	solid	Water	Salinity	temperature
#	g	G	TDS mg/L	degree C
1	15	100	22.1	28.2
2	15	100	21.1	26.9

Appendix F: Resedimentation procedure

Slurry Preparation:

1. Measure 300g Kaolin powder, 13.68g sea salt and 390g water.
2. Dissolve the salt in the water completely.
3. Mixing the solution with the Kaolinite powder thoroughly until it is homogenous. It takes about 20 minutes.

De-airing Process

1. Prepare a 1L flask as the container for the slurring.
2. Attach a vacuum pump to a small flask with crystal (dryer). Place a filter between the pump and flask.
3. Connect the 1L flask with the small flask with the rubber tube.
4. Turn on the vacuum and use the free end to suck up the slurring into the tube.
5. Seal off the free end tubing by a stopper.
6. Let the vacuum pump run until all air bubbles disappear (about 45 minutes)

Pouring the slurry into the consolidometer

Use a funnel and rubber extension tube to pour the de-aired slurry into the consolidometer.

Additional weights

The loading stress at different stages are shown in **Table F.1**

Table F.1: Loading stress at different stage

load number	added mass	total mass
#	(g)	(g)
0	60	60
1	60	120
2	120	240
3	250	490
4	500	990
5	1000	1990
6	2000	3990
7	4000	7990
8	8000	15990
9	10000	25990
10	12000	37990
unload	-28500	9490

Appendix G: Results from Constant-rate-of-strain test

FIGURES

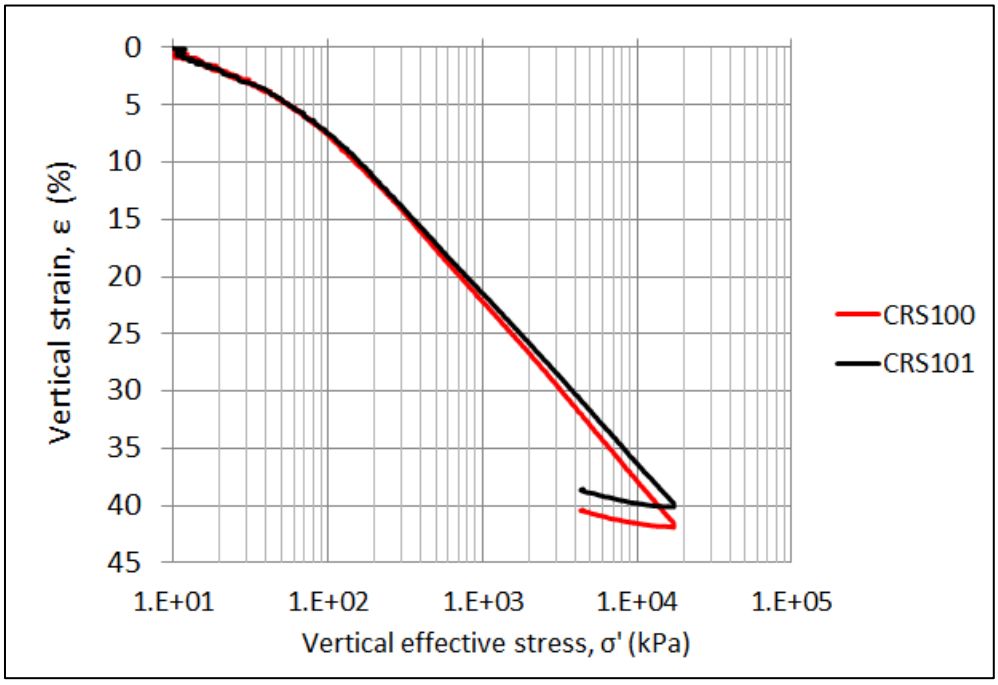

Figure G.1: Vertical strain vs. Vertical effective stress

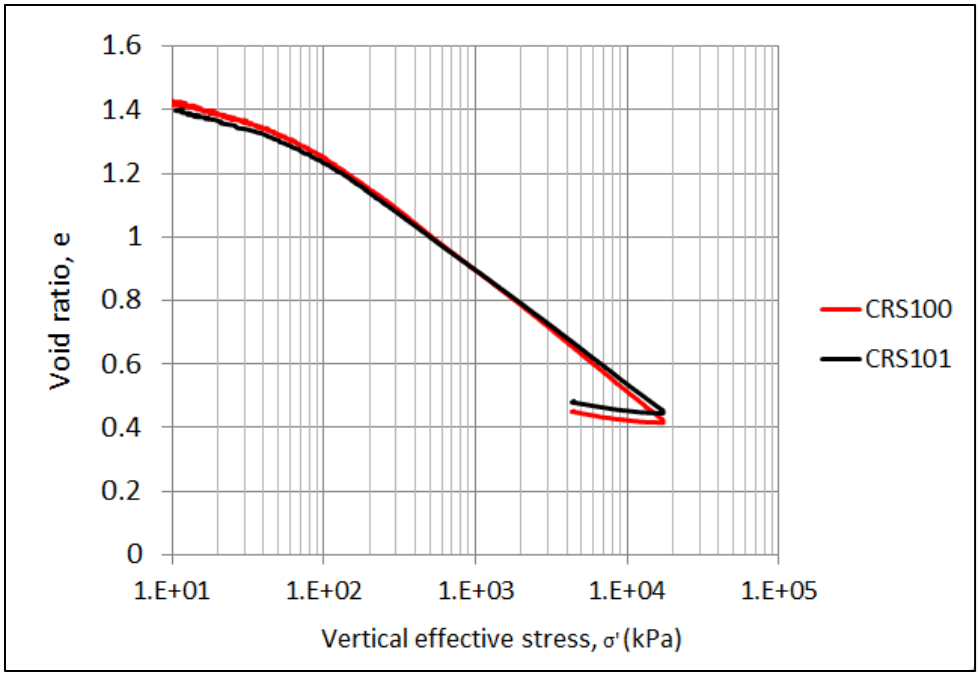

Figure G.2: Void ratio vs. vertical effective stress

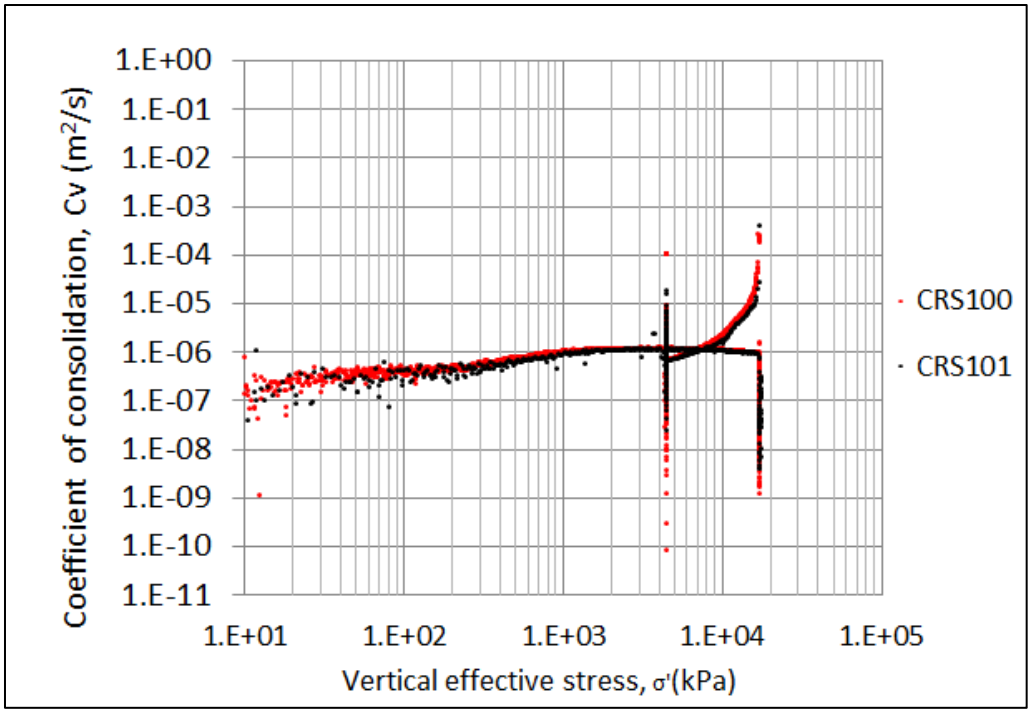

Figure G.3: Coefficient of consolidation vs. Vertical effectives stress

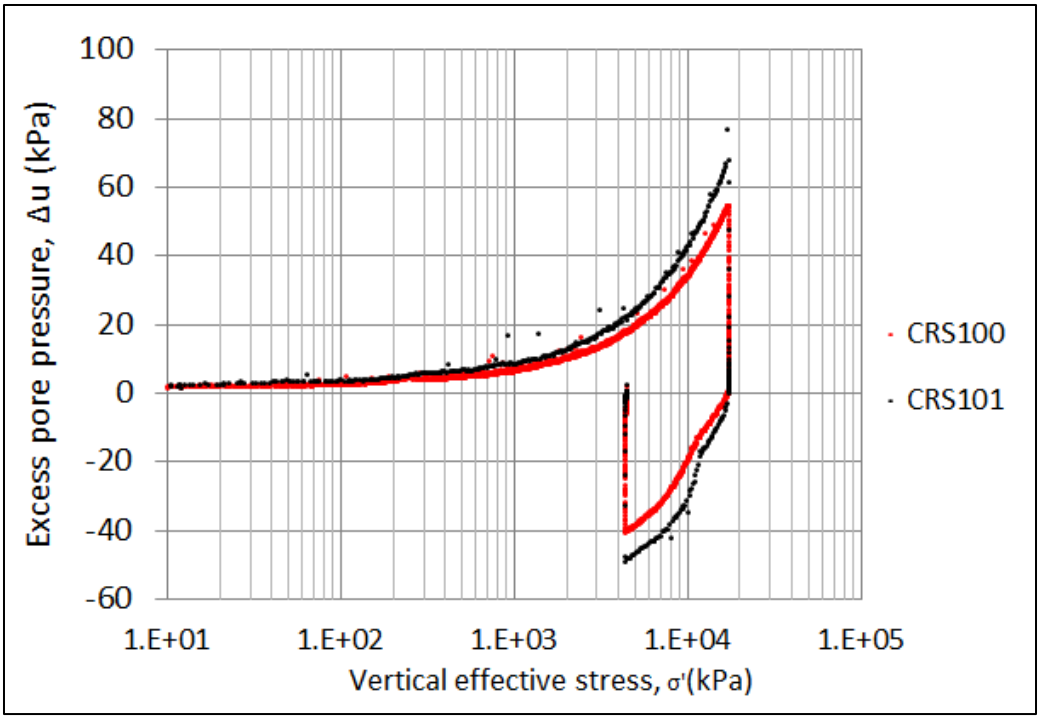

Figure G.4: Excess pore pressure vs. Vertical effectives stress

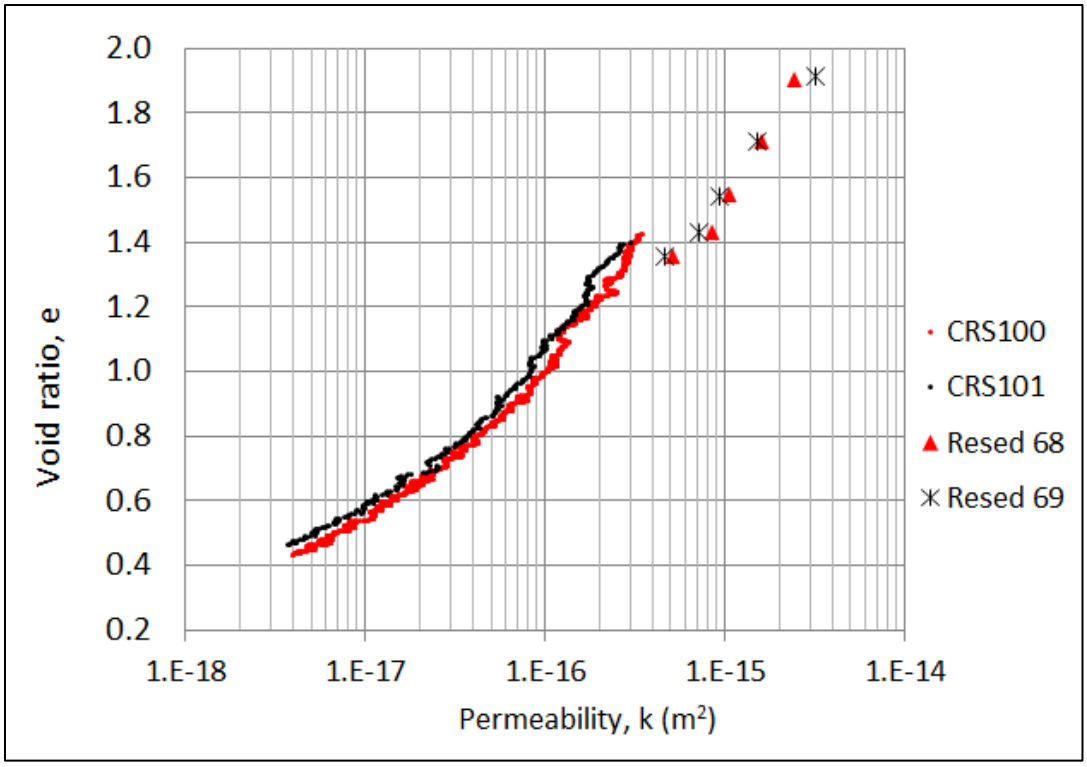

Figure G.5: Void ratio vs. Permeability

Bibliography

ASTM, 2005. Standard Test Methods for Liquid Limit, Plastic Limit, and Plasticity Index of Soils, in: International, A. (Ed.), D 4318-05, West Conshohocken, PA, p. 16.

ASTM, 2006. Standard test method for one-dimensional consolidation properties of saturated cohesive soils using controlled-strain loading (Standard D4186-06), in: 04.08), A.B.o.A.S.V. (Ed.), Soil and Rock (I). American Society for Testing and Materials, West Conshohocken, PA, p. 15.

ASTM, 2007. Standard test method for particle-size analysis of soils (Standard D422-63R07), in: 04.08), A.B.o.A.S.V. (Ed.), Soil and Rock (I). American Society for Testing and Materials, West Conshohocken, PA, pp. 10-17.

Barker, C., 1972. Aquathermal Pressuring--Role of Temperature in Development of Abnormal-Pressure Zones: GEOLOGICAL NOTES. AAPG Bulletin 56, 2068-2071.

Barker, C., 1990. Calculated Volume and Pressure Changes During the Thermal Cracking of Oil to Gas in Reservoirs (1). AAPG Bulletin 74, 1254-1261.

Betts, S.W., 2013. Compressibility and permeability of Gulf of Mexico Mudrocks. Resedimented and In-Situ (Mater Thesis)

Blanpied, M.L., Lockner, D.A., Byerlee, J.D., 1992. An earthquake mechanism based on rapid sealing of faults. Nature 358, 574-576.

Brehoeft, J.D., Hanshaw, B., 1968. On the maintenance of anomalous fluid pressures: I. Thick sedimentary sequences. Geological Society of America Bulletin 79, 1097-1106.

Bruce, C.H., 1984. Smectite dehydration--its relation to structural development and hydrocarbon accumulation in northern Gulf of Mexico basin. AAPG Bulletin 68, 673-683.

Burst, J.F., 1969. Diagenesis of Gulf Coast clayey sediments and its possible relation to petroleum migration. AAPG Bulletin 53, 73-93.

Byerlee, J., 1990. Friction, overpressure and fault normal compression. Geophys. Res. Lett 17, 2109-2112.

Cosgrove, J.W., 2001. Hydraulic fracturing during the formation and deformation of a basin: a factor in the dewatering of low-permeability sediments. AAPG Bulletin 85, 737-748.

Czerniak, M., 2011. The role of permeability weighting in centroid positioning Geopressure Annual Meeting.

Dickinson, G., 1953. Geological aspects of abnormal reservoir pressures in Gulf Coast Louisiana. AAPG Bulletin 37, 410-432.

Dugan, B., Flemings, P., 2002. Fluid flow and stability of the US continental slope offshore New Jersey from the Pleistocene to the present. Geofluids 2, 137-146.

Dugan, B., Flemings, P.B., Olgaard, D.L., Gooch, M., 2003. Consolidation, effective stress, and fluid pressure of sediments from ODP Site 1073, US mid-Atlantic continental slope. Earth and Planetary Science Letters 215, 13-26.

Elsworth, D., Voight, B., 1995. Dike intrusion as a trigger for large earthquakes and the failure of volcano flanks. JOURNAL OF GEOPHYSICAL RESEARCH-ALL SERIES-100, 6005-6005.
Flemings, P.B., Lupa, J.A., 2004. Pressure prediction in the Bullwinkle Basin through petrophysics and flow modeling (Green Canyon 65, Gulf of Mexico). Marine and Petroleum Geology 21, 1311-1322.
Flemings, P.B., Stump, B.B., Finkbeiner, T., Zoback, M., 2002. Flow focusing in overpressured sandstones: Theory, observations, and applications. American Journal of Science 302, 827-855.
Garenstroom, L., TROMP, R.A.J., de JONG, M.C., BRANDENBURG, A.M., 1993. Overpressures in the Central North Sea: implications for trap integrity and drilling safety. Geological Society, London, Petroleum Geology Conference series 4, 1305-1313.
Gibson, 1958. The progress of consolidation in a clay layer increasing in thickness with time.
Gordon, D.S., Flemings, P.B., 1998. Generation of overpressure and compaction-driven fluid flow in a Plio-Pleistocene growth-faulted basin, Eugene Island 330, offshore Louisiana. Basin Research (1998) 10, 177–196.
Hantschel, T., Kauerauf, A.I., 2009. Fundamentals of basin and petroleum systems modeling. Springer.
Harrison, W.J., Summa, L.L., 1991. Paleohydrology of the Gulf of Mexico basin. American Journal of Science 291, 109-176.
Holman, W.E., Robertson, S.S., 1994. Field development, depositional model, and production performance of the turbiditic" J" sands at prospect Bullwinkle, Green Canyon 65 field, outer-shelf Gulf of Mexico, Submarine Fans and Turbidite Systems: SEPM Foundation, Gulf Coast Section, 15th Annual Bob Perkins Research Conference. SEPM, pp. 425-437.
Hunt, J.M., 1990. Generation and Migration of Petroleum from Abnormally Pressured Fluid Compartments (1). AAPG Bulletin 74, 1-12.
Kevin, D. Best., 2002. Development of an Integrated Model for Compaction/Water Driven Reservoirs and its Application on the J1 and J2 Sands at Bullwinkle, Green Canyon Block 65, Deepwater Gulf of Mexico (Master Thesis)
Lambe, T., Whitman, R., 1979. Soil Mechanics, SI Version, J. Wiley and Sons, New York.
Law, B.E., Spencer, C., 1998. Memoir 70, Chapter 1: Abnormal Pressure in Hydrocarbon Environments.
Long, H., Flemings, P.B., Germaine, J.T., Saffer, D.M., 2011. Consolidation and overpressure near the seafloor in the Ursa Basin, Deepwater Gulf of Mexico. Earth and Planetary Science Letters 305, 11-20.
Mello, U.T., Karner, G.D., Anderson, R.N., 1994. A physical explanation for the positioning of the depth to the top of overpressure in shale-dominated sequences in the Gulf Coast basin, United States. Journal of Geophysical Research 99, 2775-2789.
Powley, D., 1990. Pressures and hydrogeology in petroleum basins. Earth-Science Reviews 29, 215-226.

Prather, B. E., J. R. Booth, G. S. Steffens, and P. A. Craig, 1998, Classification, lithologic calibration, and stratigraphic succession of seismic facies of intraslope basins, deep-waterGulf of Mexico: American Association of Petroleum Geologists Bulletin, v. 82, Issue 5A, p. 701-728.
Prior, D.B., Coleman, J.M., 1982. Active slides and flows in underconsolidated marine sediments on the slopes of the Mississippi delta. Marine slides and other mass movements, 21-49.
Reilly, M.J., Flemings, P.B., 2010. Deep pore pressures and seafloor venting in the Auger Basin, Gulf of Mexico. Basin Research 22, 380-397.
Saffer, D.M., 2003. Pore pressure development and progressive dewatering in underthrust sediments at the Costa Rican subduction margin: Comparison with northern Barbados and Nankai. Journal of Geophysical Research 108, 2261.
Schneider, J., Flemings, P.B., Dugan, B., Long, H., Germaine, J.T., 2009. Overpressure and consolidation near the seafloor of Brazos-Trinity Basin IV, northwest deepwater Gulf of Mexico. Journal of Geophysical Research 114, B05102.
Seldon, B., Flemings, P.B., 2005. Reservoir pressure and seafloor venting: Predicting trap integrity in a Gulf of Mexico deepwater turbidite minibasin. AAPG Bulletin 89, 193-209.
Spencer, C.W., 1987. Hydrocarbon generation as a mechanism for overpressuring in Rocky Mountain region. AAPG Bulletin 71, 368-388.
Snedden, John W., Peter J. Vrolijk, Larry T. Sumpter, Mike L. Sweet, Kevin R. Barnes, Elijah White, M.Ellen Meurer, 2007, Reservoir Connectivity: Definitions, Strategies, and Applications: International Petroleum Technical Conference: IPTC 11375 MS, 7 pages and figures.
Stigall, J., Dugan, B., 2010. Overpressure and earthquake initiated slope failure in the Ursa region, northern Gulf of Mexico. Journal of Geophysical Research 115, B04101.
Terzaghi, K., Peck, R.B., Mesri, G., 1996. Soil mechanics in engineering practice. Wiley-Interscience.
Van Rensbergen, P., Depreiter, D., Pannemans, B., Moerkerke, G., Van Rooij, D., Marsset, B., Akhmanov, G., Blinova, V., Ivanov, M., Rachidi, M., Magalhaes, V., Pinheiro, L., Cunha, M., Henriet, J.-P., 2005. The El Arraiche mud volcano field at the Moroccan Atlantic slope, Gulf of Cadiz. Marine Geology 219, 1-17.
Yang, Y., Aplin, A.C., 2004. Definition and practical application of mudstone porosity–effective stress relationships. Petroleum Geoscience 10, 153-162.
Yang, Y., Aplin, A.C., 2010. A permeability–porosity relationship for mudstones. Marine and Petroleum Geology 27, 1692-1697.
Yardley, G.S., Swarbrick, R.E., 2000. Lateral transfer: a source of additional overpressure? Marine and Petroleum Geology 17, 523-537.